Computers and Mathematics with Applications 71 (2016) 1089–1113

Contents lists available at ScienceDirect

Computers and Mathematics with Applications

journal homepage: www.elsevier.com/locate/camwa

An analysis and an affordable regularization technique for the spurious force oscillations in the context of direct-forcing immersed boundary methods

M. Belliard [a,b,*], M. Chandesris [a,c], J. Dumas [a,d], Y. Gorsse [a,d], D. Jamet [a,d], C. Josserand [e], B. Mathieu [a,c]

[a] Commissariat à l'énergie atomique et aux énergies alternatives, CEA, DEN/DANS/DM2S/STMF/LMEC, France
[b] CEA Cadarache, Bâtiment 1222, F-13108 Saint Paul-lez-Durance Cedex, France
[c] CEA Grenoble, Bâtiment 10.05, 17 rue des Martyrs, F-38054 Grenoble Cedex 9, France
[d] CEA Saclay, Bâtiment 454, F-91191 Gif-sur-Yvette Cedex, France
[e] Institut Jean le Rond d'Alembert, Université Pierre et Marie Curie, Tour 55-65, 4 place Jussieu, 75252 Paris Cedex 05, France

ARTICLE INFO

Article history:
Received 4 June 2015
Received in revised form 9 October 2015
Accepted 24 January 2016
Available online 16 February 2016

Keywords:
Immersed boundary method
Direct forcing method
Moving body
Spurious force oscillations
Second order accurate numerical method
Fluid–structure interaction problems

ABSTRACT

The framework of this paper is the improvement of direct-forcing immersed boundary methods in presence of moving obstacles. In particular, motivations for the use of the Direct Forcing (DF) method can be found in the advantage of a fixed computational mesh for fluid–structure interaction problems. Unfortunately, the direct forcing approach suffers a serious drawback in case of moving obstacles: the well known spurious force oscillations (SFOs). In this paper, we strengthen previous analyses of the origin of the SFO through a rigorous numerical evaluation based on Taylor expansions. We propose a remedy through an easy-to-implement regularization process (regularized DF). Formally, this regularization is related to the blending of the Navier–Stokes solver with the interpolation, but no modification of the numerical scheme is needed. This approach significantly cuts off the SFOs without increasing the computational cost. The accuracy and the space convergence order of the standard DF method are conserved. This is illustrated on numerical and physical validation test cases ranging from the Taylor–Couette problem to a cylinder with an imposed sinusoidal motion subjected to a cross-flow.

1. Introduction

Fluid–structure interaction (FSI) problems are widely present in industrial applications as aircraft wings, heat-exchanger tube bundles, bridges, off-shore platforms, …. But they are tricky to simulate due to the complexity of the physical phenomena at stake and the presence of time varying geometries. For instance, the heat-exchanger tube bundles of the nuclear industry are subject to fluid–elastic coupling forces, which depend on the bundle geometry, the fluid nature (single-phase or two-phase) and on the fluid velocity. To manage numerically these complex problems, it would be tempting to use the well-known body-fitted approach. In this case, the boundary conditions (BC), that are critical for FSI issues, are exactly imposed on the fluid–structure interface. The Arbitrary Lagrangian Eulerian framework is a prototype of this

* Corresponding author at: Commissariat à l'énergie atomique et aux énergies alternatives, CEA Cadarache, DEN/DER/SESI/LEMS, Bât. 1222, F-13108 Saint Paul-lez-Durance Cedex, France. Tel.: +33 0 4 42 25 23 17; fax: +33 0 4 42 25 48 58.
E-mail address: michel.belliard@cea.fr (M. Belliard).

http://dx.doi.org/10.1016/j.camwa.2016.01.024
0898-1221/

class of methods, see for instance [1,2]. However accurate this approach may be, it is sometimes not possible to use it to handle complex industrial problems involving large motions and/or deformations of the bodies, eventually with topological changes, which require complex numerical schemes to deal with the re-meshing issue and particular geometries.

Another approach consists in using Fictitious Domain Methods [3]. The general idea is to consider only a fluid domain in which the solid boundaries are immersed. This can be done by the local modification of the computational scheme or by adding a supplementary term in the governing equations of the fluid. For the former class of methods, we can cite the Immersed Interface Method [4], the "Cut-Cell" or Cartesian Grid methods [5,6] and the Jump Embedded Boundary Condition approach [7,8]. Among other ones, well known methods of the second class of methods are the Immersed Boundary (IBM) [9] and the Ghost Cell Methods [10,11], the Fictitious Domain Method based on the explicit use of Lagrange multipliers [12], the Penalty methods [13–16], the FAT boundary method [17] and the Finite Cell Method [18]. These techniques greatly reduce the computational cost because re-meshing is in principle not required as there is only fluid cells. Concerning the IBM, this class of non-boundary conforming techniques has been first introduced by Peskin [9] in order to simulate the incompressible blood flow in a human heart by adding a vectorial supplementary term, referred to as the forcing term. This continuous term is based on a Dirac delta function smeared over a stencil of few Cartesian nodes, in the continuous Navier–Stokes equations. Following Peskin's works about elastic structures, several IB-like methods for the Immersed Boundaries (IB), with different kinds of forcing terms have been proposed in the literature, such as the continuous Feedback Forcing (FF) of Goldstein et al. [19]. In this virtual-boundary method, the forcing term is spread over the immersed boundary and can be viewed as a force density. However, the FF term depends on the flow history and, due to large values of the stiffness coefficients, its application is limited when considering BC on rigid structures. The Direct Forcing (DF) method is an alternative approach proposed by Mohd-Yusof [20] and then adapted by Fadlun et al. [21]. It consists in directly applying the desired boundary conditions on the Cartesian nodes in the fluid near the fluid–solid interface (through the characteristic function of the solid), leading to a sharp representation. Thanks to this formulation, the forcing term can be easily computed as it does not depend on the flow history [21]. The accuracy of this method lies in the direct forcing numerical scheme itself because the calculation of the forcing term is based on the discretized form of the governing equations. Since Mohd-Yusof, the DF method has been successfully applied to various FSI problems, cf. [22–33,11,34–36] for instance. As we would like to simulate complex FSI problems, such as the fluid–elastic instability of the heat-exchanger tube bundles, we have adopted the DF approach due to its simplicity of implementation and the low associated computational cost.

One undesirable property of IBM is the generation of spurious force oscillations (SFOs) [24,28–31,33,36,34] when dealing with moving bodies on a fixed computational grid. It is observed for all type of IBM, including discrete [29] and distributed [36] forcing term methods or ghost-cell methods [30,31,34]. SFOs degrade the quality of solutions and the computation of the stress forces near the fluid–solid interface. Therefore, whatever the considered IBM, one has to deal with these SFOs in order to simulate moving bodies under prescribed or flow induced movement. In the literature, it is reported that the main source of the SFO is the temporal discontinuity in the velocity at the grid points, called dead cells, where fluid becomes solid due to the body motion [33,36]. The magnitude of the spurious force oscillations, mainly attributed to the pressure (through the velocity divergence), are said to decrease with the decrease of the space-step Δx and the increase of the time-step Δt as $\mathcal{O}(\frac{\Delta x^{\alpha}}{\Delta t})$ with α a power-law coefficient [33,34]. Magnitude of the SFO also decreases when using a carefully designed discrete delta function [24,28]. Forcing into the solid (including dead cells) [29] are known to reduce the SFO without suppressing them.

Few techniques have been proposed to reduce these spurious force contributions and can be classified in two categories. On the one hand, one preferentially works on the immersed boundary conditions of the momentum balance equation. With the solid volume fraction as weight, Kajishima et al. [22] avoid the spurious pressure oscillations. Using a referential linked to the solid, Kim and Choi [25] eradicate the SFO, but their technique is devoted to a unique solid. Luo et al. [30,31] propose an implicit hybridization (through an iterative method) of the flow-solver numerical scheme and of the IBM in order to deal with the free-dead cell transitions and Chiu et al. [32] replace the algebraically-interpolated method by a differentially interpolated method. On the other hand, one may prefer working on the immersed boundary conditions of the mass balance equation. Kim et al. [37] and Lee et al. [33] combine a DF approach and an extra mass source term in the mass balance equation. This minimizes the pressure oscillations coming from the spatial discontinuities of the pressure near the IB when fresh cells (cells in the fluid and previously in the obstacle) are released. Seo et al. [34] conjointly use a DF ghost-cell method [11] for the Navier–Stokes equations and a cut-cell approach to design the pressure solver. Lee and You [35] combine the same ghost-cell method and the Kim et al. approach.

This work is twofold. First, it is devoted to the analysis of the SFO. Through numerical experiments and theoretical analysis, we confirm previous findings [33,36] that designate the dead-cell contribution as the main source of the SFO. This is stated too from the confrontation of the SFOs and the fresh-cell apparition occurrences. We propose in this paper a more formal derivation of the magnitude order of the SFO as $\mathcal{O}(\frac{\Delta x^2}{\Delta t}) + \mathcal{O}(\Delta x)$ for a first-order in space interpolation. Using rigorous numerical evaluations based on Taylor expansions, we produce the specific contributions depending on the kind of considered cells (dead, fresh or unchanged). Secondly, this work provides a practical remedy to SFOs using a regularization technique for the DF method. In the philosophy of the hybridization approach promoted by Luo et al. [30,31] or of the differentially interpolated method [32], we realize an explicit weighted mixing between the interpolation scheme and a blind version (without obstacles) of the flow solver. In fact, our method differs from that of Luo et al. by an explicit forcing term (no iteration), leaving the *native* numerical scheme unchanged, and by the determination of the weight. The former

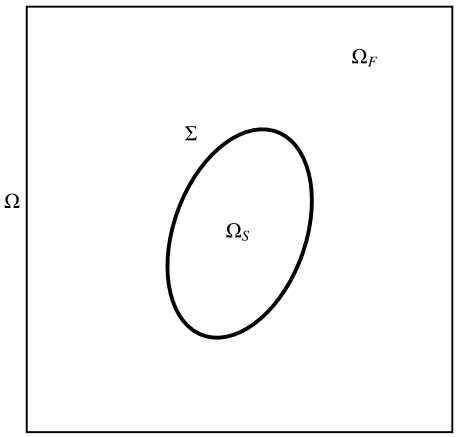

Fig. 1. Schematic representation of the computational domain Ω and the fluid–solid interface $\Sigma = \partial\Omega_F \cap \partial\Omega_S$.

property is very useful to introduce the DF method in previously existing industrial codes. Formally, it leads to a weighting of the forcing term that can be understood as the definition of a regularized characteristic function of the solid. Unlike [22], this weighting is not restricted to the solid volume fraction only. Its design is mainly led by the search of a smooth transition between the Navier–Stokes velocities and the forced velocities in the vicinity of the IB. As in [30,31], the method retains the sharp-interface representation of the solid body surface.

In practice, we only modify the characteristic functions of the obstacles and consider the standard explicit DF method. Under CFL restriction, only one strip of fresh or dead cells can appear during a time step. All the cells inside the obstacles are forced. Moreover using a non-incremental projection scheme [38,39], we compute the pressure and the velocity correction through all the fictitious domain (fluid and solid).

For clarity purpose, our presentation is done in 2-dimension space. But, that does not constitute a restriction of the method which is actually carried out in 3-D.

We first present in Section 2 the fluid governing equations, the numerical scheme, the DF method and, following Introïni et al. [40], the interpolation schemes used to implement it with order one or two in space. Then, the SFO origins are numerically analyzed on the Seo and Mittal test case [34] in Section 3. The $\mathcal{O}(\frac{\Delta x^2}{\Delta t}) + \mathcal{O}(\Delta x)$ dependency, coming from the dead cells, is theoretically demonstrated in an original way for the first-order in space version of the standard DF. Following the results of this analysis, we propose in Section 4 what we call the regularized (RG) approach. This approach, easy to implement, significantly cuts off the SFOs without increasing the computational cost and conserves the accuracy and the space convergence order. With the same assumptions as before, we theoretically show that the magnitude order of the SFO varies as $\mathcal{O}(\Delta x + \Delta t)$ in the case of the RG DF. Confirming our analysis, numerical and physical validations of the standard DF and RG DF approaches are conducted in Section 5 on various test cases ranging from the Taylor–Couette problem to a cylinder with an imposed sinusoidal motion subjected to a cross-flow.

2. Governing equations and numerical method

2.1. Governing equations

This paper deals with incompressible flows around moving solid obstacles. The full domain is named $\Omega = \Omega_F \cup \Omega_S$, where Ω_F is the fluid domain and Ω_S the solid one, and the fluid–solid interface is indicated by Σ, see Fig. 1.

The governing equations used to describe unsteady incompressible flows are given by:

$$\begin{aligned} \frac{\partial \underline{u}}{\partial t} + \nabla \cdot (\underline{u} \otimes \underline{u}) + \frac{1}{\rho}\underline{\nabla} p - \nu \nabla^2 \underline{u} = \underline{f} \quad & \text{in } \Omega_F \\ \nabla \cdot \underline{u} = 0 \quad & \text{in } \Omega_F \\ \underline{u} = \underline{u}_S \quad & \text{on } \Sigma \end{aligned} \tag{1}$$

with initial condition in Ω and boundary conditions on $\partial\Omega$. The variable $\underline{u}$ is the fluid velocity, ν the kinematic viscosity, p the pressure, ρ the fluid density, $\underline{f}$ the volume force (taken to zero hereafter) and $\underline{u}_S$ the fluid–solid interface velocity.

The knowledge of the local fluid force $\rho\nu(\underline{\underline{\nabla u}} + \underline{\underline{\nabla^t u}}) \cdot \underline{n} - p\underline{n}$ or of its integration $\oiint_{\Omega_S}(\rho\nu(\underline{\underline{\nabla u}} + \underline{\underline{\nabla^t u}}) \cdot \underline{n} - p\underline{n})\mathrm{d}\Sigma$ on the fluid–solid interface Σ allows to access the dynamic of the body if not prescribed. In turn, this body motion induces a change in the flow structure. Although crucial for the fluid–structure interaction, this point is not discuss in this paper.

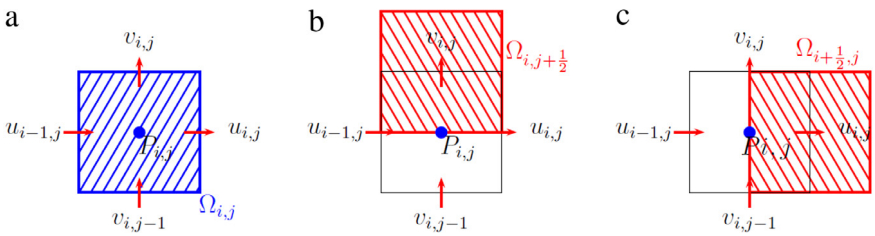

Fig. 2. Staggered arrangement of the unknowns on a 2-D Cartesian cell $(i; j)$ with the CVs of pressure ((a), blue □) and the CVs of velocity components ((b) and (c), red □). (For interpretation of the references to color in this figure legend, the reader is referred to the web version of this article.)

2.2. Spatial discretization and numerical method

The equations are discretized on a uniform Cartesian mesh using a finite volume approach with a staggered grid arrangement of the variables $(\underline{u}, P)$. As a result, the pressure degrees of freedom are located at the cell centers whereas those of each velocity component are placed at the middle of the cell edges as presented in Fig. 2. The governing equations (1) are integrated over each control volume ensuring conservation of mass and momentum balance. Here, the convection and diffusion terms are respectively approached by the QUICK and centered schemes [41].

A non-incremental fractional-step scheme is used to solve the incompressible Navier–Stokes equations. The fractional step method or projection method was introduced by Chorin and Temam in 1968–1969 for incompressible flows [38,39]. On the basis of their work, several variants have been proposed and the reader is referred to Guermond [42] for a recent overview of these methods. In L_∞ norm, the rate of convergence in time of the non-incremental version is theoretically first-order [42].

2.3. Direct forcing approach

As previously discussed in the introduction, there are several types of immersed boundary method (IBM) [9,19–21]. They all consist in computing flows around complex geometrical shapes (static/moving/deforming bodies) by immersing the physical domain Ω_F in a simpler fictitious one Ω. The presence of embedded time-varying geometry Ω_S in the computational domain Ω is taken into account thanks to a source term $\underline{F}_{IBM}$ that is added in the Navier–Stokes equations (1). In this work, the domain Ω_S is discretized through a 3-D Lagrangian triangulation. At the end of each time step, the Lagrangian mesh is moved following the fluid–solid interface velocity.

Following the direct forcing (DF) method developed in [20,21], a discrete source term $\underline{F}_{DF}$ imposes immersed boundary conditions for the flow in the vicinity of the obstacles and is added in the discretized Navier–Stokes equations (here, fully explicit for the sake of the presentation) as follows:

$$\frac{\underline{u}^{n+1} - \underline{u}^n}{\Delta t} + \nabla_h \cdot (\underline{u}^n \otimes \underline{u}^n) + \frac{1}{\rho}\underline{\nabla_h} p^{n+1} - \nu \nabla_h^2 \underline{u}^n = \underline{F}_{DF} \quad \text{in } \Omega \tag{2}$$

$$\nabla_h \cdot \underline{u}^{n+1} = 0 \quad \text{in } \Omega \tag{3}$$

where the subscript $\bullet_h$ stands for discrete operators (omitted hereafter). The source term $\underline{F}_{DF}$ refers to a direct forcing term [21] and is defined by:

$$\underline{F}_{DF} = \chi_{\mathrm{m}} \frac{\underline{u}_{\mathrm{m}} - \underline{u}^\star}{\Delta t} \quad \text{in } \Omega, \tag{4}$$

where $\underline{u}^\star$ is the predicted velocity of the fractional-step scheme without IB, χ_{m} is the characteristic function of the imposed velocities domain Ω_I^{m}, which is different depending on the considered model, and $\underline{u}_{\mathrm{m}} = \underline{u}_{\mathrm{m}}(\underline{u}_S, \underline{u}^\star)$ is the imposed velocity resulting from the adopted reconstruction model. Following the authors, the reconstruction model may be Lagrange interpolations following the grid directions [21] or in a multi-direction approach [37], the normal direction to the body surface [26], power law interpolations [27] or least squares interpolations [43]. In the rest of the paper, the subscript m means "model" that can be "base" (first order in space model) or "linear" (second order in space model).

The resolution of Eqs. (2)–(3) is split according to the following algorithm:

Step 1: Computation of the predicted velocity $\underline{u}^\star$ without taking into account the immersed boundary conditions:

$$\frac{\underline{u}^\star - \underline{u}^n}{\Delta t} + \nabla \cdot (\underline{u}^n \otimes \underline{u}^n) - \nu \nabla^2 \underline{u}^n = \underline{0} \quad \text{in } \Omega. \tag{5}$$

Step 2: Computation of the imposed velocity and the forcing term (see Sections 2.3.1 and 2.3.2):

$$\underline{u}_{\mathrm{m}} = \underline{u}_{\mathrm{m}}(\underline{u}_S, \underline{u}^\star); \qquad \underline{F}_{DF} = \chi_{\mathrm{m}} \frac{\underline{u}_{\mathrm{m}} - \underline{u}^\star}{\Delta t}. \tag{6}$$

Step 3: Addition of the direct forcing term:

$$\tilde{\underline{u}} = \underline{u}^{\star} + \Delta t \underline{F}_{DF}. \tag{7}$$

Step 4: Projection:

$$\frac{1}{\rho}\Delta p^{n+1} = \frac{1}{\Delta t}\nabla \cdot \tilde{\underline{u}} \quad \text{in } \Omega. \tag{8}$$

Step 5: Correction:

$$\underline{u}^{n+1} = \tilde{\underline{u}} - \frac{\Delta t}{\rho}\underline{\nabla} p^{n+1} \quad \text{in } \Omega. \tag{9}$$

In the following section we detail the interface models used to calculate the imposed velocities.

2.3.1. The base model

The simplest approach to implement this IBM is to consider a first order accurate in space method. As for the ghost cell approach [10], we choose to only force velocities that are inside the solid domain, depicted by red diamonds in Fig. 3. Due to this formulation, $\Omega_l^{\text{base}} = \Omega_S$ and χ_{base} is defined as follows:

$$\chi_{\text{base}}(\underline{x}) = \begin{cases} 1 & \text{if } d(\underline{x}) \geq 0 \\ 0 & \text{otherwise} \end{cases}$$

where $d(\underline{x})$ is the signed distance function to the fluid–solid interface with $d(\underline{x}) \geq 0$ inside Ω_S. At the beginning of the time step, the signed distance is computed in 3-D using the barycenters and the external normal vectors of the Lagrangian-mesh faces. In this formulation, the imposed velocity is the solid velocity:

$$\underline{u}_{\text{base}}(\underline{x}) := \underline{u}_S(\underline{x}). \tag{10}$$

With a Cartesian grid, the base model leads to a stepwise description of the immersed interface Σ.

2.3.2. The linear model

A way to improve the spatial order of the method is to use an interpolation scheme to reconstruct the velocity field near the interface. This is the most widely employed approach in the literature [21] and we have adopted the procedure developed by Introïni et al. [40]. The linear model consists in using an interpolation scheme to calculate the fluid velocities located near Σ. More precisely, Ω_l^{linear} is divided into two sub-domains as depicted in Fig. 3. The first one is made up of the velocities located inside Ω_S that are forced to $\underline{u}_S$ as for the base model. The second one must contain at least the fluid velocities having a neighbor in Ω_S and are forced using an interpolation scheme to guaranty the second order global accuracy. Such a domain can be defined by adding a Δx-thickness layer to the solid domain, leading to the following expression of χ_{linear}:

$$\chi_{\text{linear}}(\underline{x}) = \begin{cases} 1 & \text{if } d(\underline{x}) \geq -\Delta x \\ 0 & \text{otherwise} \end{cases}$$

where Δx is the cell length. Then, $\underline{u}_{\text{linear}}$ takes the following form:

$$\underline{u}_{\text{linear}}(\underline{x}) := \begin{cases} \underline{u}_{\text{int}}(\underline{x}) & \text{if } -\Delta x \leq d(\underline{x}) < 0 \\ \underline{u}_S(\underline{x}) & \text{if } d(\underline{x}) \geq 0 \end{cases} \tag{11}$$

where $\underline{u}_{\text{int}}$ is the velocity obtained with a linear interpolation scheme, second order accurate in space. In this interpolation scheme, the fluid contribution is built through an averaged reconstruction of the velocity gradient near Σ and the solid contribution is determined by means of a minimization problem, see [40].

This model is illustrated in Fig. 3, where the red-diamond velocities are forced to the solid velocity (as for the base model) and the green-triangle ones to interpolated velocities (these velocities are free when considering the base model).

3. An analysis of the spurious force oscillations

This part is dedicated to the analysis of the origin of the SFO and to the mathematical evaluation of its magnitude. First of all, we introduce the SFO through the Seo and Mittal test case [34]. As already mentioned, without restriction on the space dimension d, dependency on $\mathcal{O}(\frac{\Delta x^2}{\Delta t})$ was notified by Lee et al. [33] through a second-order interpolation. Considering only the mass balance equation, Seo and Mittal theoretically demonstrated dependency on $\mathcal{O}(\frac{\Delta x^d}{\Delta t})$ [34]. In this work, we mainly focus on the momentum balance equation. Then using Taylor expansions of the forcing term and of the velocity near the IB, we quantify each specific contribution to the SFO magnitude coming from the dead, fresh or unchanged cells. Finally numerical studies give confirmation of this power-law.

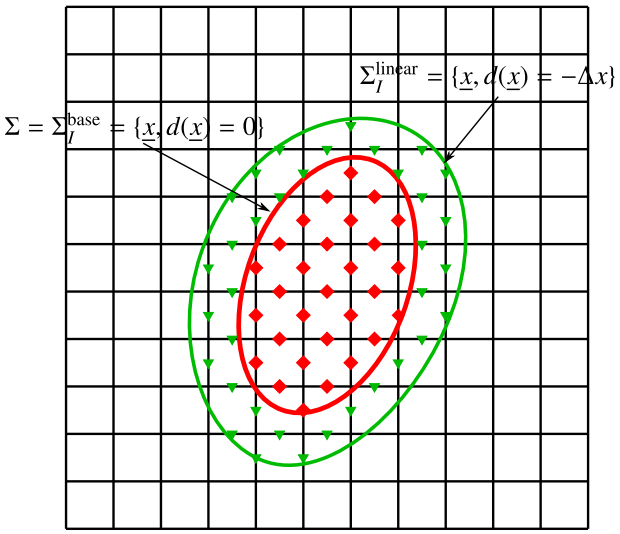

Fig. 3. Schematic representation of the base and the linear model on a staggered grid. The red diamonds represent the velocities forced to the solid velocity and the green triangles are the ones forced to the interpolated velocity for the linear model. (For interpretation of the references to color in this figure legend, the reader is referred to the web version of this article.)

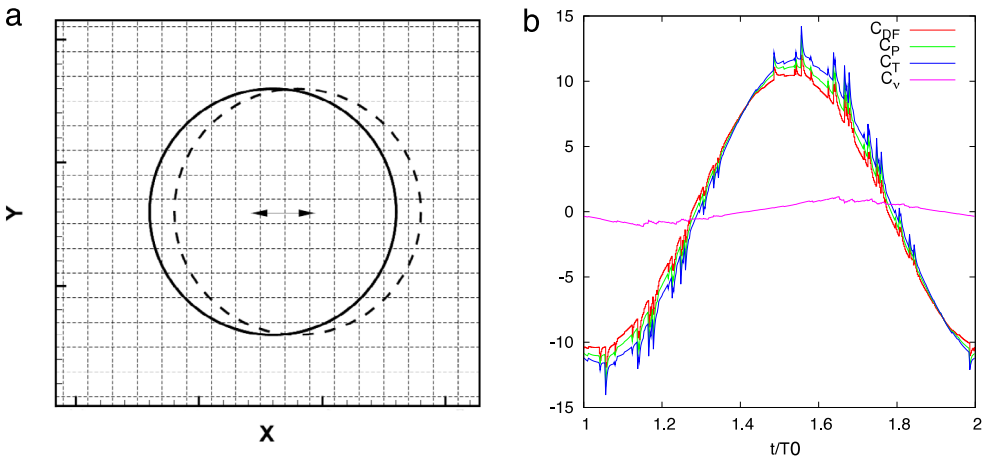

Fig. 4. Seo and Mittal's test case [34]: (a) geometry and computational grid (zoom around the obstacle) and (b) physical dimensionless coefficients time histories: C_P, C_v, C_T and C_{DF}. Computation done with the DF base model, cf. Section 2.3.1.

3.1. Seo and Mittal test case

In order to introduce the issue of the generation of spurious force oscillations, when using a DF approach for a rigid moving body, the simple test case of Seo and Mittal [34] is considered. It consists in a circular cylinder centered at the coordinates (x_c, y_c) of diameter D which oscillates sinusoidally along the x-direction in a fluid at rest:

$$\begin{cases} x_c(t) = x_c(0) + X_0(1 - \cos(2\pi f_0 t)) \\ y_c(t) = y_c(0) \end{cases}$$

where $(x_c(0), y_c(0))$ are the initial coordinates of the cylinder center, X_0 is the amplitude of the oscillation and f_0 is its frequency (see Fig. 4(a) for a schematic representation). The period of oscillation is $T_0 = \frac{1}{f_0}$.

The computational domain is a $4D \times 4D$ square with the upper and lower boundaries set to no-slip walls, homogeneous Neumann conditions for the pressure and the velocity on the left and right sides, $(x_c(0), y_c(0)) = (2D, 2D)$ and $X_0 = 0.125D$. Due to the cylinder motion, the cylinder maximum velocity is $U_0 = X_0 2\pi f_0$, the Reynolds and Strouhal numbers, respectively defined by $Re = \frac{U_0 D}{\nu}$ and $St = \frac{f_0 D}{U_0}$ are set to 78.5 and 1.27.

In SFO studies, we are interested in the temporal variations of the following physical dimensionless coefficients: the pressure drag C_P, the friction drag C_v and the total drag C_T. They are the components along the x-axis of the pressure,

viscosity and the total force. In addition, we consider the total contribution of the direct forcing term C_{DF}. These coefficients are defined as follow:

$$\underline{C_P} = \frac{\oiint_{\Omega_S} -p\underline{n}\mathrm{d}\Sigma}{0.5\rho D^3 f_0^2} \tag{12}$$

$$\underline{C_\nu} = \frac{\oiint_{\Omega_S} \rho\nu(\underline{\underline{\nabla u}} + \underline{\underline{\nabla^t u}}) \cdot \underline{n}\mathrm{d}\Sigma}{0.5\rho D^3 f_0^2} \tag{13}$$

$$\underline{C_T} = \underline{C_P} + \underline{C_\nu} \tag{14}$$

$$\underline{C_{DF}} = \frac{\iiint_{\Omega_S} \rho\underline{F_{DF}} \cdot \underline{e_x}\mathrm{d}\Omega}{0.5\rho D^3 f_0^2}. \tag{15}$$

By integrating the Navier–Stokes equations including the forcing term, C_{DF} is linked to C_T by the following expression:

$$C_T = -C_{DF} + \frac{\left(\iiint_{\Omega_S} \rho\left(\frac{\partial \underline{u}}{\partial t} + \nabla\cdot(\underline{u}\otimes\underline{u})\right)\mathrm{d}\Omega\right)\cdot\underline{e_x}}{0.5\rho D^3 f_0^2}. \tag{16}$$

The volume space integration of Eq. (15) or Eq. (16) is numerically done on the imposed-velocity domain Ω_I^m and not on the exact solid domain Ω_s. We use the velocity control volumes of our FV scheme, cf. Fig. 2. The surface space integration of Eq. (12) or Eq. (13) is not done on the exact interface $\partial\Omega_s$ but on the approximated fluid–solid interface Σ_I^m using the velocity-control-volume faces included in Σ_I^m. As the pressure and the Cauchy stress are defined on these faces, we directly use the terms involved in the momentum balance equation.

To illustrate the SFO phenomena, the problem is first solved on a 64^2 uniform grid with a fixed time-step $\Delta t = 0.002\frac{1}{f_0} = 0.002T_0$, corresponding to the following CFL number 0.025, where $CFL = \frac{U_0\Delta t}{\Delta x}$ and Δx is the grid spacing. Considering this grid, the cylinder diameter is spanned by 16 grid points. The computation is performed with the DF method described in Section 2.3. The evolution over a period T_0 of the dimensionless coefficients of interest are presented in Fig. 4(b). It is important to point out that it is mainly the pressure drag component that is disturbed by the spurious oscillations whereas the time history of the friction drag is almost regular. Therefore, the SFOs are in fact due to the spurious pressure oscillations (SPO). Then, it is also interesting to notice that C_{DF} is nearly equal to C_T.

Then, the convergence in space is investigated by considering a fixed time-step $\Delta t = \Delta t_0 = 0.002T_0$, with four uniform grids (64^2, 128^2, 192^2 and 256^2 cells), leading to the following CFL numbers: 0.025, 0.05, 0.1 and 0.2. Thus, on these four grids, the cylinder diameter D is spanned by 16, 32, 48 and 64 grid points, respectively.

The convergence in time is investigated by considering a 64^2-cell grid and the following time-steps $\Delta t = \Delta t_0$, $2\Delta t_0$, $4\Delta t_0$ and $8\Delta t_0$, leading to the following CFL numbers: 0.025, 0.05, 0.1 and 0.2. Fig. 5(a) and (b) display the C_P time histories over a period of time. Qualitatively, they demonstrate that the pressure oscillations decreases with decreasing grid spacing and with increasing time-step, as mentioned in [33,34].

3.2. Theoretical analysis of the SFO origin

We analyze the SFO origin in the case of the DF base model described in Section 2.3.1. First of all, we assume the origin is located in the forcing steps (2. and 3.) between the prediction (1.) and the projection steps (4.) of this algorithm. Indeed, due to the nature itself of the DF approach, the projections (4) and correction steps (5.) are blind to the solid boundary as they do not take directly into account the solid boundaries for their computation. However, the projection step spreads the pressure oscillations over all the computational domain via the source term of the Poisson equation which can be disturbed because of the forcing step.

As previously shown on Seo and Mittal's test case, C_{DF} and C_P are disturbed by equivalent spurious oscillations. In order to quantify the amplitude of these oscillations, it is assumed a constant solid velocity in space and time (the analysis remains valid for regular variations). This assumption allows Taylor expansions on the velocity field in time and space. For the sake of simplicity, we assume a CFL number smaller than unity and the following hypothesis:

$$\Omega_{s,h}^{n-1} = \Omega_{s,h}^{n} \neq \Omega_{s,h}^{n+1} \tag{17}$$

where $\Omega_{s,h}^n$ is the set of velocities forced at the time-step n. Eq. (17) means that all the velocities forced at the time-step n were already forced at the time-step $n-1$ even if that usually does not hold for two consecutive steps in real life. But it enables a mere simplification of the analysis consistent with a limited-space presentation. However, it is not essential to the computations as it will be stated below. This reduces the inventory of the different cells categories following their history with respect to the forcing term. The velocity evolution between the time-steps n and $n+1$ is schematically described as follow:

$$\underline{u}^n \xrightarrow[\mathcal{O}(\Delta t)]{\Delta t RHS^n(\underline{u}^n)} \underline{u}^{\star,n} \xrightarrow[\mathcal{O}(\Delta t)]{\Delta t\underline{F_{DF}}} \tilde{\underline{u}} \xrightarrow[\mathcal{O}(\Delta t)]{-\frac{\Delta t}{\rho}\nabla p^{n+1}} \underline{u}^{n+1} \xrightarrow[\mathcal{O}(\Delta t)]{\Delta t RHS^{n+1}(\underline{u}^{n+1})} \underline{u}^{\star,n+1} \tag{18}$$

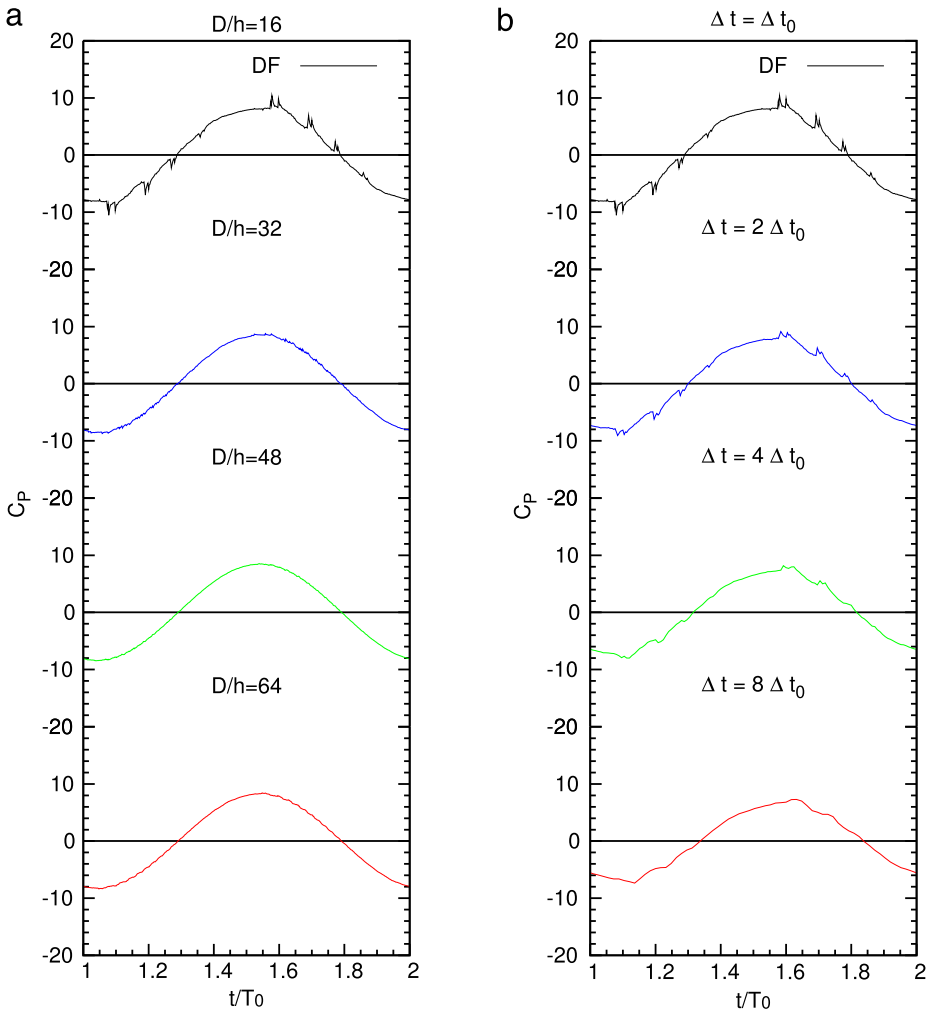

Fig. 5. C_P time histories for the Seo and Mittal's test case: (a) $\Delta t = \Delta t_0 = 0.002T_0$ for different grid spacing and (b) $D/\Delta x = 16$ for different time-steps.

where $\Delta t RHS^n(\underline{u}^n)$ denotes the explicit Navier–Stokes solver of the prediction step (1.). One can measure the DF term variation, between the time-steps n and $n+1$, by calculating:

$$\int_{\Omega_{s,h}^{n+1}} \underline{F}_{DF}^{n+1} \mathrm{d}\Omega - \int_{\Omega_{s,h}^{n}} \underline{F}_{DF}^{n} \mathrm{d}\Omega = \int_{\Omega_{s,h}^{n+1}\cap\Omega_{s,h}^{n}} \underline{F}_{DF}^{n+1} - \underline{F}_{DF}^{n} \mathrm{d}\Omega + \int_{\Omega_{s,h}^{n+1}\setminus\Omega_{s,h}^{n}} \underline{F}_{DF}^{n+1} \mathrm{d}\Omega - \int_{\Omega_{s,h}^{n}\setminus\Omega_{s,h}^{n+1}} \underline{F}_{DF}^{n} \mathrm{d}\Omega. \tag{19}$$

By expressing the integrals at the discrete level and writing the DF term expression, the above equation becomes:

$$\begin{aligned}\int_{\Omega_{s,h}^{n+1}} \underline{F}_{DF}^{n+1} \mathrm{d}\Omega - \int_{\Omega_{s,h}^{n}} \underline{F}_{DF}^{n} \mathrm{d}\Omega = &\sum_{K\in\Omega_{s,h}^{n+1}\cap\Omega_{s,h}^{n}} \frac{\underline{u}_S - \underline{u}^{\star,n+1} - \underline{u}_S + \underline{u}^{\star,n}}{\Delta t}\Delta x^d \\ &+ \sum_{K\in\Omega_{s,h}^{n+1}\setminus\Omega_{s,h}^{n}} \frac{\underline{u}_S - \underline{u}^{\star,n+1}}{\Delta t}\Delta x^d - \sum_{K\in\Omega_{s,h}^{n}\setminus\Omega_{s,h}^{n+1}} \frac{\underline{u}_S - \underline{u}^{\star,n}}{\Delta t}\Delta x^d\end{aligned} \tag{20}$$

where K is a mesh element and Δx^d the volume of a cell in d dimension. Denoting FC (fresh cell) the set of velocities that became freshly fluid ($K \in \Omega_{s,h}^{n}\setminus\Omega_{s,h}^{n+1}$) and DC (dead cell) the set of velocities that became freshly forced ($K \in \Omega_{s,h}^{n+1}\setminus\Omega_{s,h}^{n}$), we get:

$$\int_{\Omega_{s,h}^{n+1}} \underline{F}_{DF}^{n+1} \mathrm{d}\Omega - \int_{\Omega_{s,h}^{n}} \underline{F}_{DF}^{n} \mathrm{d}\Omega = \frac{\Delta x^d}{\Delta t}\left(\sum_{K\in\Omega_{s,h}^{n+1}\cap\Omega_{s,h}^{n}} \left(\underline{u}^{\star,n} - \underline{u}^{\star,n+1}\right) + \sum_{DC}\left(\underline{u}_S - \underline{u}^{\star,n+1}\right) - \sum_{FC}\left(\underline{u}_S - \underline{u}^{\star,n}\right)\right). \tag{21}$$

Forced cells at n and n + 1. $\left(\underline{u}^{\star,n} - \underline{u}^{\star,n+1}\right)$ is associated to the velocities forced at time-steps n and $n+1$. Thanks to Eq. (18), $\underline{u}^{\star,n+1} = \underline{u}^{n+1} + \mathcal{O}(\Delta t) = \tilde{\underline{u}}^{n} + \mathcal{O}(\Delta t) = \underline{u}_S + \mathcal{O}(\Delta t)$. By doing the same analysis and thanks to the assumption (17), $\underline{u}^{\star,n} = \underline{u}_S + \mathcal{O}(\Delta t)$. Therefore:

$$\underline{u}^{\star,n} - \underline{u}^{\star,n+1} = \mathcal{O}(\Delta t). \tag{22}$$

Dead cells. $\left(\underline{u}_S - \underline{u}^{\star,n+1}\right)$ is associated to velocities free at n and forced at $n+1$. As this velocity is forced at $n+1$, it has at least one forced neighbor at the previous time-step n as we assumed $CFL < 1$. In addition, the DF base model is of order one in space, implying that $\underline{u}^{\star,n+1} = \underline{u}^{\star,n+1}_{\text{Forced neighbor}} + \mathcal{O}(\Delta x)$ where $\underline{u}^{\star,n+1}_{\text{Forced neighbor}} = \underline{u}_S + \mathcal{O}(\Delta t)$. Thus:

$$\underline{u}^{\star,n+1} - \underline{u}_S = \mathcal{O}(\Delta x) + \mathcal{O}(\Delta t). \tag{23}$$

Fresh cells. $\left(\underline{u}_S - \underline{u}^{\star,n}\right)$ is associated to velocities forced at n and free at $n+1$. As these velocities were previously forced at $n-1$ due to the assumption (17), $\underline{u}^{\star,n} = \underline{u}^{n} + \mathcal{O}(\Delta t) = \underline{u}_S + \mathcal{O}(\Delta t)$. Thus:

$$\underline{u}_S - \underline{u}^{\star,n} = \mathcal{O}(\Delta t). \tag{24}$$

Conclusion. Finally, the number of FCs and DCs increases with the mesh size. These cells appear by a layer of thickness adjacent to the boundary (dimension 1 in 2D and dimension 2 in 3D). Their number is proportional to $(\frac{D}{\Delta x})^{d-1} = \mathcal{O}(\frac{1}{\Delta x^{d-1}})$. The number of cells forced at the time-steps n and $n+1$ increases at the same rate as the mesh elements proportional to $(\frac{D}{\Delta x})^{d} = \mathcal{O}(\frac{1}{\Delta x^{d}})$. As last with the assumption (17):

$$\begin{aligned}
\int_{\Omega^{n+1}_{s,h}} \underline{F}^{n+1}_{DF} \mathrm{d}\Omega - \int_{\Omega^{n}_{s,h}} \underline{F}^{n}_{DF} \mathrm{d}\Omega &= \frac{\Delta x^d}{\Delta t}\left(\mathcal{O}\left(\frac{\Delta t}{\Delta x^d}\right) + \mathcal{O}\left(\frac{\Delta t + \Delta x}{\Delta x^{d-1}}\right) + \mathcal{O}\left(\frac{\Delta t}{\Delta x^{d-1}}\right)\right) \\
&= \underbrace{\mathcal{O}(1)}_{K\in\Omega^{n+1}_{s,h}\cap\Omega^{n}_{s,h}} \underbrace{+\mathcal{O}(\Delta x) + \mathcal{O}\left(\frac{\Delta x^2}{\Delta t}\right)}_{K\in DC} + \underbrace{\mathcal{O}(\Delta x)}_{K\in FC} \\
&= \mathcal{O}(1) + \mathcal{O}(\Delta x) + \mathcal{O}\left(\frac{\Delta x^2}{\Delta t}\right).
\end{aligned} \tag{25}$$

This analysis can also be conducted without the assumption (17). But it would have been necessary to distinguish the velocities free at $n-1$ that are forced at n and the velocities already forced at $n-1$. However for the sake of clarity this development is not exposed as the conclusions are exactly the same.

As the value of the term $\mathcal{O}(\frac{\Delta x^2}{\Delta t})$ can be big, specially for small Δt, we can guess that the DCs play the principal role in the SFO. But as the coefficients of the various contributions are unknown, we cannot confidently predict whether the DCs or the FCs are the main contribution to the SFO. To remove this uncertainty Fig. 6 displays the time history of the forcing term maximum, the number of DCs and FCs with the numerical conditions of Section 3.1. Fig. 6(a) shows that the forcing term oscillations occur at the same times as new cells enter in the solid domain and become dead cells. Whereas, on Fig. 6(b) it can be noted that the fresh cells do not trigger significant oscillations as no time coincidence can be found between the FC's occurrence and the forcing term maximum. This means the DCs are the main source of pressure oscillations (at least for small time-steps). The FC contributions are commonly attributed to space discontinuities of the velocity and the pressure [33]. Here the non-incremental pressure-projection scheme and the computation of velocities and pressures over the whole fictitious domain should contribute to reduce this space discontinuity for FCs.

Then thanks to Eq. (25), for small values of the time-step and the DF method with a first-order interpolation, SFOs are proportional to $\mathcal{O}(\frac{\Delta x^2}{\Delta t})$. Through a more formal derivation, giving the specific contributions of each kind of cells (dead, fresh or unchanged), we generalize here the Lee et al. expression $\mathcal{O}(\frac{\Delta x^2}{\Delta t})$ [33], based on simple considerations concerning the velocity change for dead cells.

Theoretical analysis of the SFO magnitude using the linear DF was not conducted here. But the numerical experiments described in Section 4.3 conduct to a power-law about $\mathcal{O}(\frac{\Delta x^3}{\Delta t})$ for small time-steps.

3.3. Numerical validation on SFO

As above mentioned, Eq. (25) is consistent with the expression $\mathcal{O}(\frac{\Delta x^\alpha}{\Delta t})$ found in the literature. However, it can be interesting to point out that the biggest is the time-step the more the oscillations tend to be dependent on $\mathcal{O}(\Delta x)$ instead of $\mathcal{O}(\frac{\Delta x^2}{\Delta t})$. Taking into account all the specific contributions, the present analysis brings an extra light into the behavior of the SFO amplitude. This point is numerically illustrated here.

The pressure 2δ-discontinuity, noted $C_P^{2\delta}$ and introduced by Seo and Mittal [34], is used to obtain quantitative results. It is defined by the following equation:

$$C_P^{2\delta} = C_P^{n+1} - 2C_P^{n} + C_P^{n-1} \tag{26}$$

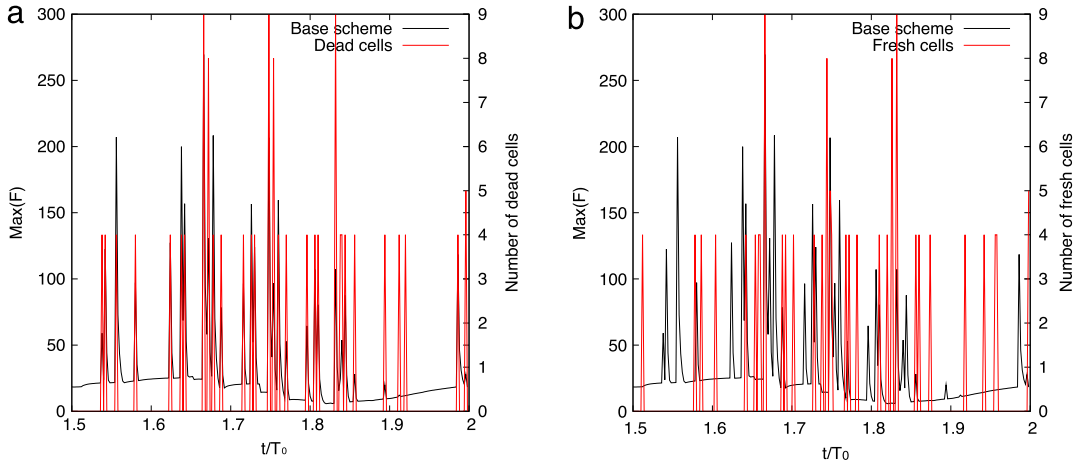

Fig. 6. Forcing term maximum for the Seo and Mittal's test case (m/s^2). DC and FC numbers on the left and right sides.

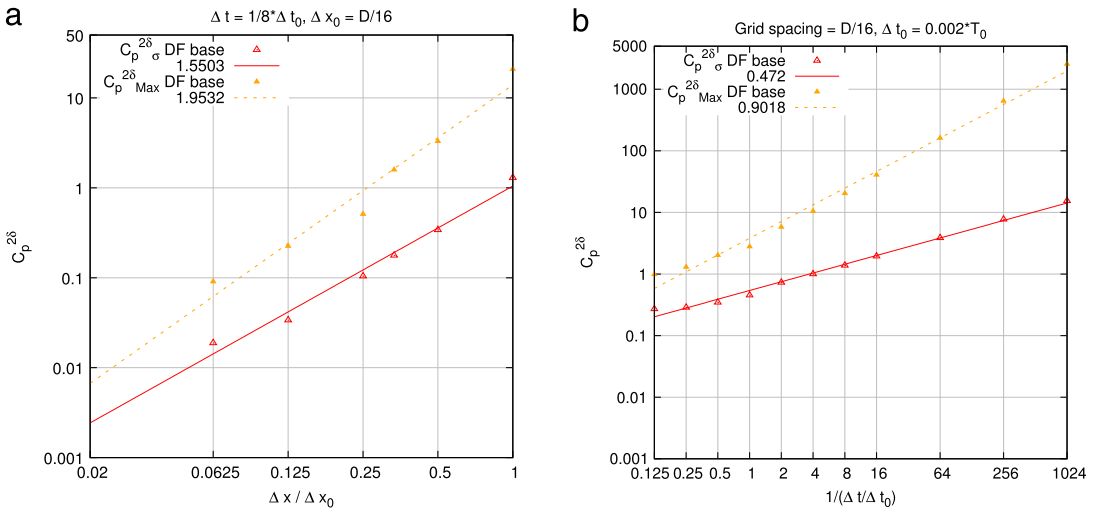

Fig. 7. $C_{P,\sigma}^{2\delta}$ and $C_{P,Max}^{2\delta}$ for the Seo and Mittal's test case versus: (a) grid spacing ($\Delta t = \frac{1}{8}\Delta t_0$) or (b) time-steps ($D/\Delta x = 16$).

where n is the time-step index. The maximum and the standard deviation values of $C_P^{2\delta}$, noted $C_{P,Max}^{2\delta}$ and $C_{P,\sigma}^{2\delta}$, are calculated over a period of time. Let us notice than $C_{P,\sigma}^{2\delta}$ is bounded by $C_{P,Max}^{2\delta}$. Using the same numerical parameters as in Section 3.1, the results are plotted in Fig. 7(a) and (b) as a function of grid spacing and time-step size. A power-law fitting gives:

$$C_{P,Max}^{2\delta} = \frac{\Delta x^{1.9532}}{\Delta t^{0.9018}} \quad \text{and} \quad C_{P,\sigma}^{2\delta} = \frac{\Delta x^{1.5503}}{\Delta t^{0.472}}. \tag{27}$$

The result obtained for $C_{P,Max}^{2\delta}$ is in very good agreement with Eq. (25). In Fig. 7(b), it is interesting to notice that when the time-step increases (corresponding to the left side of the picture), $C_{P,\sigma}^{2\delta}$ and $C_{P,Max}^{2\delta}$ tend to decrease slower with the time-step than for the smallest time-step (right side of the picture). This original result is well described by our theoretical analysis summarized by Eq. (25), because the contribution of the DCs is $\mathcal{O}(\Delta x) + \mathcal{O}(\frac{\Delta x^2}{\Delta t})$. So when Δt increases, $\mathcal{O}(\frac{\Delta x^2}{\Delta t})$ decreases and the contributions in $\mathcal{O}(\Delta x)$ of the DCs and FCs become significant in comparison with $\mathcal{O}(\frac{\Delta x^2}{\Delta t})$. At the opposite, when the time-step is very small the contribution in $\mathcal{O}(\frac{\Delta x^2}{\Delta t})$ of the DCs is much higher than the other ones.

$C_{P,\sigma}^{2\delta}$ is quite close to the theoretical result also. It is necessary to have in mind that the maximum of $C_P^{2\delta}$ quantifies mainly the oscillations triggered by the DCs. This explains the behavior difference between $C_{P,\sigma}^{2\delta}$ and $C_{P,Max}^{2\delta}$. Indeed, as the main source of oscillations, the DCs are at the origin of the biggest peaks (which are the maximums), whereas the FC contribution is much lower. It is why $C_{P,Max}^{2\delta}$ is rather close to the predicted DC variation $\mathcal{O}(\frac{\Delta x^2}{\Delta t})$. The standard deviation measures the dispersion of $C_P^{2\delta}$. Thus, $C_{P,\sigma}^{2\delta}$ quantifies all the oscillations contributions (FC and DC). Therefore, it cannot have a variation following exactly the one of the maximums.

4. The direct forcing regularized formulation

Analysis of Section 3 done with the base model predicts a SFO behavior in $\mathcal{O}(\frac{\Delta x^2}{\Delta t}) + \mathcal{O}(\Delta x)$ due to dead cells. Considering coarse to moderate grids and small to moderate time-steps (precisely the configuration where the SFOs are annoying) the power-law is $\mathcal{O}(\frac{\Delta x^2}{\Delta t})$. Numerical studies give confirmations of this power-law. A simple way to tackle the oscillations would be to decrease the grid-spacing and increase the time-step. However, that would be at the expense of the computational time when decreasing the grid-spacing and at the expense of the precision when increasing the time step. Consequently it cannot be an end in itself. To reduce the DC contributions to the spurious pressure oscillations, the mass balance can be corrected (e.g. [37,34]) or the imposed velocities can be carefully computed taking into account the Navier–Stokes solver (e.g. [30,31]). These methods (cut-cell method for mass balance, fully-implicit hybridization of interpolated and Navier–Stokes velocities, …) are efficient but quite invasive considering for instance an industrial computer code already using a standard DF method. That is why a regularized (RG) formulation of the direct forcing, called the RG DF approach, easy to implement and capable of cutting off efficiently the oscillations without any extra computational time, is presented.

Through a regularization process, it is possible to reduce the SFO by roughly an order of magnitude in comparison with the original DF approach. Moreover, the $\mathcal{O}(\Delta x) + \mathcal{O}(\frac{\Delta x^2}{\Delta t})$ dependency of the SFO amplitude, with first-order in space interpolation, is changed to $\mathcal{O}(\Delta x) + \mathcal{O}(\Delta t)$. This change in the power-law is very interesting for small time-steps. To the knowledge of the authors, it was not achieved by the past (e.g. the power-law is not changed when using the method described in [34]).

First, we focus on the numerical method and analyze its impact on the spurious force oscillations. Then, we numerically study the space and time convergence of the oscillation amplitude on the Seo and Mittal's test case using the RG DF.

4.1. Numerical method

In the standard DF method, the added force $\underline{F}_{DF}$ is defined through the use of a Heaviside-like generalized function for χ_{m}, cf. Eq. (4), resulting in a "all or nothing" method and a sharp transition of the forcing term through the free-to-forced velocity interface. Moreover, when a free-velocity grid point is crossed by this interface, unless a specific treatment, no consistency in time is guaranteed between the previous Navier–Stokes solver value and the new interpolated one, contributing to the SFO apparition. Luo et al. [30,31] and Chiu et al. [32] propose such kind of treatment to improve this time consistence for a ghost cell method, taking into account the Navier–Stokes solver in the design of the interpolation scheme. Here, the key idea of the RG DF formulation is, for a new given forced-velocity point, to smooth the transition between the values given by the Navier–Stokes solver and by the interpolation (or affectation) scheme.

Considering a fluid forced-velocity point in Ω_f^m, we propose the following new formulation for the discretized imposed velocity, now denoted by $\underline{u}_i$ to distinguish from the interpolated one $\underline{u}_{\mathrm{m}}$:

$$\begin{cases} \underline{u}_i = \xi_{\mathrm{m}}\underline{u}_{\mathrm{m}} + (1-\xi_{\mathrm{m}})\underline{u}^\star \\ \underline{F}_{RG} = \dfrac{\underline{u}_i - \underline{u}^\star}{\Delta t} \end{cases} \tag{28}$$

where $\xi_{\mathrm{m}}(\underline{x})$ is a regular function of the signed distance $d(\underline{x})$. This formulation is named "regularized" (RG) because, for the degrees of freedom with $0 < \xi_{\mathrm{m}} < 1$, the new imposed velocity $\underline{u}_i$ is regularized through a linear combination of the *blind* Navier–Stokes solver velocity $\underline{u}^\star$ and of the interpolated velocity $\underline{u}_{\mathrm{m}}$.

We choose to define $\xi_{\mathrm{m}}(\underline{x})$ in such a way that it varies linearly from 0 to 1 across a layer of thickness Δd centered on the iso-distance d_0^m. But different functions $\xi_{\mathrm{m}}(\underline{x})$ can be addressed. In this work, d_0^m is defined as the signed distance of the forced–free interface Σ_f^m (depending of the considered model m) and $\Delta d = \Delta x$. Hence the function expression can be interpreted as the *forced-velocity domain fraction* $\tau_{\mathrm{m}}(\underline{x})$ in the control volume of the forced-velocity point and reads as

$$\xi_{\mathrm{m}}(\underline{x}) = \frac{\Delta x + 2[d(\underline{x}) - d_0^m]}{2\Delta x} \equiv \tau_{\mathrm{m}(\underline{x})}. \tag{29}$$

This is graphically represented on Fig. 8 in 1D. As the forced–free interface Σ_f^{base} of the base model coincides with Σ ($d_0^{base} = 0$, cf. Fig. 3), this definition leads to the *solid domain fraction* $\xi_{\mathrm{base}} = \frac{\Delta x + 2d(\underline{x})}{2\Delta x} \equiv \tau(\underline{x})$. This phase-mean approach can be found in [22] for a first-order in space direct forcing method. For the linear model, the signed distance of the forced–free interface Σ_f^{linear} is $d_0^{linear} = -\Delta x$, cf. Fig. 3. Then, the function ξ_{linear} is similar to the function ξ_{base} shifted by $-\Delta x$.

From a continuous-geometry point of view, there is no difference between the standard DF method and the regularized one. From a discrete-geometry point of view, the difference lies in the discretization of the indicator of the imposed-velocity region, leading to the corresponding discretized forcing term $\underline{F}_{RG}$:

$$\underline{F}_{RG} = \xi_{\mathrm{m}}\frac{\underline{u}_{\mathrm{m}} - \underline{u}^\star}{\Delta t} \tag{30}$$

that is the standard DF forcing term $\underline{F}_{DF}$ with the generalized function χ_{m} replaced by the regular function ξ_{m}. In particular, $\underline{F}_{RG}$ has exactly the same expression as $\underline{F}_{DF}$ of the original formulation when the control volume of the fluid velocity is entirely in the forced domain (i.e.: $\xi_{\mathrm{m}} = \chi_{\mathrm{m}} = 1$).

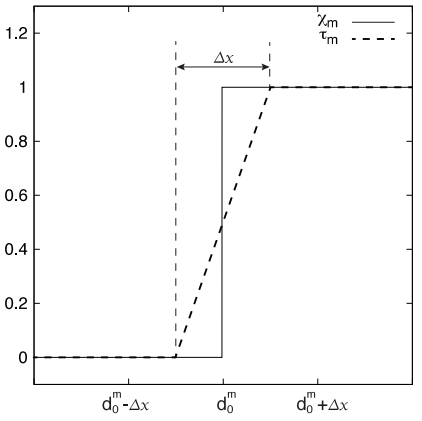

Fig. 8. Representation of $\chi_{\mathrm{m}}(x)$ and $\xi_{\mathrm{m}}(x) = \frac{\Delta x + 2[d(x) - d_0^m(x)]}{2\Delta x} \equiv \tau_{\mathrm{m}}(x)$ in 1D.

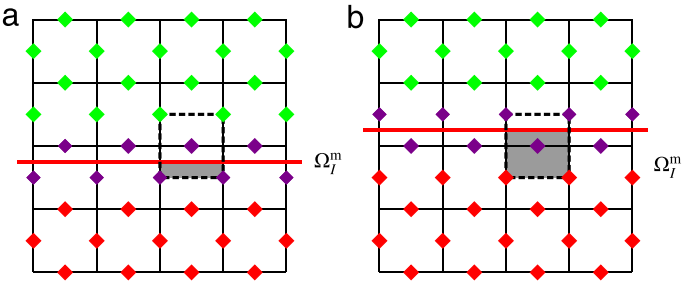

Fig. 9. Schematic representation of the regularized formulation: (a) time step n and (b) time step $n+1$. The fluid velocities located in the free domain are in green and those in the forced domain Ω_l^m are in red. The forced–free interface Σ_l^m is a red line and the velocities where their control volumes are occupied by a fraction of the forced domain are in purple. (For interpretation of the references to color in this figure legend, the reader is referred to the web version of this article.)

In a certain way, considering this ξ_{m}-weighting of the force, we can found some links with the volume-weighting of Kajishima and Takiguchi [22] or the Uhlmann method [24] leading also to a weighting of the discrete force term on the Cartesian grid. But, in the proposed regularized DF, the weighting is not restricted to the only solid volume fraction and a sharp interface is considered. In another way, similarities can be found with the Luo et al. method [30,31] in which an implicit hybridization of the flow-solver numerical scheme and of the velocity interpolation scheme is done. But here, this hybridization is explicit in time and it saves us to modify the discrete operators to include the interpolated velocity.

Practically, the implementation of Eq. (28) is:

$$\underline{u}_i = \begin{cases} \underline{u}_{\mathrm{m}} & \text{if } \xi_{\mathrm{m}} = 1 \\ \xi_{\mathrm{m}}\underline{u}_{\mathrm{m}} + (1-\xi_{\mathrm{m}})\underline{u}^{\star} & \text{if } 0 < \xi_{\mathrm{m}} < 1 \\ \underline{u}^{\star} & \text{if } \xi_{\mathrm{m}} = 0. \end{cases} \tag{31}$$

Thereby, when the solid is in motion, the fluid velocity will be forced progressively (and not abruptly as in the original DF approach) to the interpolated forced velocity $\underline{u}_{\mathrm{m}}$ as it enters in the forced domain Ω_l^m, smoothing the temporal discontinuity of the velocity through the interface. This procedure is illustrated on Fig. 9(a) with $\xi_{\mathrm{m}} = \tau_{\mathrm{m}}$. The black dashed-line square denotes a control volume occupied by a fraction τ_m^n (in gray) of the forced domain. Thus, the correspondent imposed velocity is proportional to this fraction. At the next time-step, cf Fig. 9(b), the forced domain has been vertically translated and the control volume is now occupied by a more consequent fraction $\tau_m^{n+1} > \tau_m^n$. Thus, the imposed velocity is forced proportionally to this new forced domain fraction.

All the other steps of the resolution of the incompressible Navier–Stokes equations are solved as previously exposed. As anyone can notice, the above formulation does not increase the computational time cost and is very easy to implement.

Finally, let us focus on the cut-cell mass/volume conservation with the RG approach. Including the definition (28) of the imposed-velocity $\underline{u}_i$ in the discrete $\tilde{\underline{u}}$-velocity divergence of the cut cell K, $\nabla \cdot \tilde{\underline{u}}|_K = \frac{1}{|K|}\sum_f |f|\,\underline{u}_{if} \cdot \underline{n}_f$, we get:

$$\nabla \cdot \tilde{\underline{u}}|_K = \frac{1}{|K|} \sum_{f/\xi_{\mathrm{m}f}=0} |f|\,\underline{u}^{\star}{}_f \cdot \underline{n}_f + \frac{1}{|K|} \sum_{f/\xi_{\mathrm{m}f}>0} |f|\,(\xi_{\mathrm{m}f}\,\underline{u}_{\mathrm{m}f} + (1-\xi_{\mathrm{m}f})\,\underline{u}^{\star}{}_f) \cdot \underline{n}_f \tag{32}$$

where $|K|$ stands for the measure of the cut cell and f for a face of the cell of measure $|f|$. Then, this expression can be recast into a *no-weighting* contribution and a correction q:

$$\nabla \cdot \tilde{\underline{u}}|_K = \frac{1}{|K|}\left[\sum_{f/\xi_{\mathrm{m}f}=0} |f|\,\underline{u}^{\star}{}_f \cdot \underline{n}_f + \sum_{f/\xi_{\mathrm{m}f}>0} |f|\,\underline{u}_{\mathrm{m}f} \cdot \underline{n}_f\right] - q \tag{33}$$

$$q = \frac{1}{|K|}\sum_{f/\xi_{\mathrm{m}f}>0} |f|\,(1-\xi_{\mathrm{m}f})\,(\underline{u}_{\mathrm{m}f} - \underline{u}^{\star}{}_f)\cdot \underline{n}_f. \tag{34}$$

The term with the brackets in the RHS of (33) corresponds to $\nabla \cdot \tilde{\underline{u}}|_K$ in case of the standard DF. Hence, we can consider that the RG formulation formally modifies the RHS of the pressure equation (8) by adding the source/sink term q. It differs from the Kim et al. correction [37] on the solid velocity. Considering $\xi_{\mathrm{m}} = \tau_{\mathrm{m}}$, (34) can be viewed as a fluid correction proportional to the fluid fraction $(1-\tau_{\mathrm{m}f})$ of the cut-cell faces.

4.2. Impact on the oscillations

In order to evaluate the temporal variation of the forcing term with the RG formulation, we repeat the analysis conducted on the base model in Section 3.2 by replacing $\underline{F}_{DF}$ by $\underline{F}_{RG}$ in Eq. (19)

$$\int_{\Omega^{n+1}_{s,h}} \underline{F}^{n+1}_{RG}\mathrm{d}\Omega - \int_{\Omega^{n}_{s,h}} \underline{F}^{n}_{RG}\mathrm{d}\Omega = \int_{\Omega^{n+1}_{s,h}\cap\Omega^{n}_{s,h}} \underline{F}^{n+1}_{RG} - \underline{F}^{n}_{RG}\mathrm{d}\Omega + \int_{\Omega^{n+1}_{s,h}\setminus\Omega^{n}_{s,h}} \underline{F}^{n+1}_{RG}\mathrm{d}\Omega - \int_{\Omega^{n}_{s,h}\setminus\Omega^{n+1}_{s,h}} \underline{F}^{n}_{RG}\mathrm{d}\Omega \tag{35}$$

taking into account $\xi_{\mathrm{base}} \equiv \tau$ in Eq. (30). $\Omega^{n}_{s,h}$ is the set of velocities forced at the time step n. It can be divided into two subsets. The first one is the subset of the velocities with $\tau^n = 1$ and the second one is the subset of the velocities with $0 < \tau^n < 1$. Again $\Omega^{n+1}_{s,h} \cap \Omega^{n}_{s,h}$ is the set of velocities forced at the time-steps n and $n+1$ and $\Omega^{n+1}_{s,h}\setminus\Omega^{n}_{s,h}$ is the set of velocities that were free at the time-step n ($\tau^n = 0$) but that are forced at the time-step $n+1$ ($0 < \tau^{n+1} \leq 1$). Similarly $\Omega^{n}_{s,h}\setminus\Omega^{n+1}_{s,h}$ is the set of velocities that were forced at the time-step n ($0 < \tau^n \leq 1$) and that become free at the time-step $n+1$ ($\tau^{n+1} = 0$).

By expressing the integrals at the discrete level and by writing the regularized forcing term expression, one gets:

$$\begin{aligned}\int_{\Omega^{n+1}_{s,h}} \underline{F}^{n+1}_{RG}\mathrm{d}\Omega - \int_{\Omega^{n}_{s,h}} \underline{F}^{n}_{RG}\mathrm{d}\Omega = &\sum_{K\in\Omega^{n+1}_{s,h}\cap\Omega^{n}_{s,h}} \frac{\tau^{n+1}\left(\underline{u}_S - \underline{u}^{\star,n+1}\right) - \tau^{n}\left(\underline{u}_S - \underline{u}^{\star,n}\right)}{\Delta t}\Delta x^d \\ &+ \sum_{K\in\Omega^{n+1}_{s,h}\setminus\Omega^{n}_{s,h}} \tau^{n+1}\frac{\underline{u}_S - \underline{u}^{\star,n+1}}{\Delta t}\Delta x^d - \sum_{K\in\Omega^{n}_{s,h}\setminus\Omega^{n+1}_{s,h}} \tau^{n}\frac{\underline{u}_S - \underline{u}^{\star,n}}{\Delta t}\Delta x^d.\end{aligned} \tag{36}$$

Using the notations introduced before, it comes:

$$\begin{aligned}\int_{\Omega^{n+1}_{s,h}} \underline{F}^{n+1}_{RG}\mathrm{d}\Omega - \int_{\Omega^{n}_{s,h}} \underline{F}^{n}_{RG}\mathrm{d}\Omega = \frac{\Delta x^d}{\Delta t}\Bigg(&\sum_{K\in\Omega^{n+1}_{s,h}\cap\Omega^{n}_{s,h}} \tau^{n+1}\left(\underline{u}_S - \underline{u}^{\star,n+1}\right) - \tau^{n}\left(\underline{u}_S - \underline{u}^{\star,n}\right) \\ &+ \sum_{DC} \tau^{n+1}\left(\underline{u}_S - \underline{u}^{\star,n+1}\right) - \sum_{FC} \tau^{n}\left(\underline{u}_S - \underline{u}^{\star,n}\right)\Bigg).\end{aligned} \tag{37}$$

Dead cells. $\tau^{n+1}\left(\underline{u}_S - \underline{u}^{\star,n+1}\right)$ is associated to the dead cells. That means that the velocity was free at the time-step n ($\tau^n = 0$) and is forced for the first time at the time-step $n+1$. We consider the most penalizing case where the fraction of forced domain in the control volume is maximum while it was zero at the previous time step. This occurs when $d = -\Delta x/2$ at time n, see Fig. 10(a). Indeed, the distance at time $n+1$ is $d = -\Delta x/2 + |\underline{u}_S|\Delta t$, see Fig. 10(b). Considering $\tau = \frac{\Delta x + 2d}{2\Delta x}$ (see Fig. 8), we obtain $\tau^{n+1} = \frac{U_S \Delta t}{\Delta x} \propto CFL$. A freshly forced velocity has at least one forced neighbor (located at a few Δx) entirely forced at the previous time-step. For the base model (first order in space), this implies that: $\underline{u}^{\star,n+1} = \underbrace{\underline{u}^{\star,n+1}_{\text{Entirely forced neighbor}}}_{\underline{u}_S + \mathcal{O}(\Delta t)} + \mathcal{O}(\Delta x)$.

Then:

$$\tau^{n+1}\left(\underline{u}_S - \underline{u}^{\star,n+1}\right) = \mathcal{O}\left(\frac{\Delta t}{\Delta x}\right)\left(\mathcal{O}(\Delta x) + \mathcal{O}(\Delta t)\right).$$

Fresh cells. $\tau^{n}\left(\underline{u}_S - \underline{u}^{\star,n}\right)$ is associated to the fresh cells. That means the velocity was last forced at time-step n and will be free at $n+1$. There are three possible histories for the FCs. Either there exists a time-step $n-N$ where this velocity was

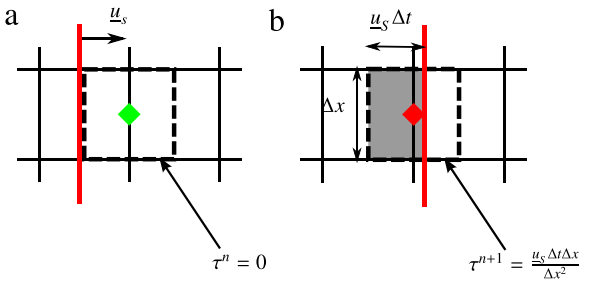

Fig. 10. Schematic representation of a dead cell.

entirely forced ($\tau^{n-N} = 1$). Or this time-step does not exist and there remains two possibilities: either it has always been partially forced, either there exists a time-step $n - N$ where it has been a DC.

Let us consider the first possible history. That means $\underline{u}^{\star,n-N+1} = \underline{u}_S + \mathcal{O}(\Delta t)$ by using Eq. (18). We reconstruct the history as follows:

$$\begin{cases} \underline{u}^{\star,n} - \underline{u}_S & = & \left(1 - \tau^{n-1}\right)\left(\underline{u}^{\star,n-1} - \underline{u}_S\right) + \mathcal{O}(\Delta t) \\ \dots & = & \dots \\ \underline{u}^{\star,n+2-N} - \underline{u}_S & = & \left(1 - \tau^{n-N+1}\right)\left(\underbrace{\underline{u}^{\star,n-N+1} - \underline{u}_S}_{\mathcal{O}(\Delta t)}\right) + \mathcal{O}(\Delta t) \end{cases}$$

and we get:

$$\underline{u}^{\star,n} - \underline{u}_S = \mathcal{O}(\Delta t) \prod_{i=1}^{N-1}\left(1 - \tau^{n-i}\right) + \mathcal{O}(\Delta t)\left(1 + \sum_{k=0}^{N-3}\prod_{j=0}^{k}\left(1 - \tau^{n-1-j}\right)\right).$$

As $\tau < 1$ due to its definition, $\prod_{i=1}^{N-1}\left(1 - \tau^{n-i}\right) < 1 = \mathcal{O}(1)$ and $\left(1 + \sum_{k=0}^{N-3}\prod_{j=0}^{k}\left(1 - \tau^{n-1-j}\right)\right) < (1 + (N-2)) = \mathcal{O}(1)$, then:

$$\left(\underline{u}^{\star,n} - \underline{u}_S\right) = \mathcal{O}(\Delta t).$$

Now, let us consider the second and third possibilities. As this velocity has been forced at n, it has at least one neighbor (at a distance of a few Δx) entirely forced at n. Thanks to the fact the base model with the RG approach is first order in space, we have:

$$\underline{u}^n = \mathcal{O}(\Delta x) + \underbrace{\underline{u}^n_{\text{Entirely forced neighbor}}}_{\underline{u}_S + \mathcal{O}(\Delta t)}$$

and therefore by using Eq. (18):

$$\left(\underline{u}^{\star,n} - \underline{u}_S\right) = \mathcal{O}(\Delta x) + \mathcal{O}(\Delta t).$$

Finally, we conclude that $\left(\underline{u}^{\star,n} - \underline{u}_S\right) = \mathcal{O}(\Delta t) + \mathcal{O}(\Delta x)$ for every FC. Regarding τ^n and using again the CFL condition, we found that τ^n is $\mathcal{O}\left(\frac{\underline{u}_S \Delta t}{\Delta x}\right)$ by similar considerations to those made for Fig. 10 ($\frac{\underline{u}_S \Delta t \Delta x}{\Delta x^2}$ is the maximum added or removed solid fraction of a control volume in one time-step). Eventually, we get:

$$\tau^n\left(\underline{u}^{\star,n} - \underline{u}_S\right) = \mathcal{O}\left(\frac{\Delta t}{\Delta x}\right)\left(\mathcal{O}(\Delta t) + \mathcal{O}(\Delta x)\right).$$

Forced cells at n and $n+1$. $\tau^{n+1}\left(\underline{u}_S - \underline{u}^{\star,n+1}\right) - \tau^n\left(\underline{u}_S - \underline{u}^{\star,n}\right)$ is associated to the velocities forced at the time-steps n and $n+1$. The set $\Omega^{n+1}_{s,h} \cap \Omega^n_{s,h}$ can be divided into three distinct subsets. The first one is the subset of the velocities with $\tau^{n-1} = \tau^n = \tau^{n+1} = 1$. The second subset is composed of the velocities with $0 < \tau^{n-1} < 1, 0 < \tau^n \leq 1$ and $0 < \tau^{n+1} \leq 1$. Finally the third subset is composed of the velocities that were fluid at $n-1$ and freshly forced at n (that are in fact the DCs at n).

For the first subset, we are exactly in the same case as for the DF base model: $\left(\underline{u}_S - \underline{u}^{\star,n+1}\right) - \left(\underline{u}_S - \underline{u}^{\star,n}\right) = \left(\underline{u}^{\star,n} - \underline{u}^{\star,n+1}\right)$. Consequently, the analysis previously conducted is still valid: $\left(\underline{u}^{\star,n} - \underline{u}^{\star,n+1}\right) = \mathcal{O}(\Delta t)$.

Let us consider the second subset. We apply exactly the same analysis as for the FCs: $\left(\underline{u}^{\star,n} - \underline{u}_S\right) = \mathcal{O}(\Delta t) + \mathcal{O}(\Delta x)$ and then we get:

$$\tau^{n+1}\left(\underline{u}_S - \underline{u}^{\star,n+1}\right) - \tau^n\left(\underline{u}_S - \underline{u}^{\star,n}\right) = \mathcal{O}\left(\frac{\Delta t}{\Delta x}\right)\left(\mathcal{O}(\Delta t) + \mathcal{O}(\Delta x)\right).$$

Finally the velocities of the third subset are DCs at the time-step n. As previously done, we get: $\left(\underline{u}^{\star,n} - \underline{u}_S\right) = (\mathcal{O}(\Delta t) + \mathcal{O}(\Delta x))$ that leads to:

$$\tau^{n+1}\left(\underline{u}_S - \underline{u}^{\star,n+1}\right) - \tau^n\left(\underline{u}_S - \underline{u}^{\star,n}\right) = \mathcal{O}\left(\frac{\Delta t}{\Delta x}\right)(\mathcal{O}(\Delta t) + \mathcal{O}(\Delta x)).$$

Conclusion. For the same reasons previously exposed, concerning the number of DFs and DCs, we obtain:

$$\begin{aligned}
&\int_{\Omega_{s,h}^{n+1}} \underline{F}_{RG}^{n+1} \mathrm{d}\Omega - \int_{\Omega_{s,h}^{n}} \underline{F}_{RG}^{n} \mathrm{d}\Omega \\
&= \frac{\Delta x^d}{\Delta t}\left[\mathcal{O}\left(\frac{\Delta t}{\Delta x^d}\right) + \mathcal{O}\left(\frac{\Delta t}{\Delta x}\frac{(\Delta t + \Delta x)}{\Delta x^{d-1}}\right) + \mathcal{O}\left(\frac{\Delta t}{\Delta x}\frac{(\Delta t + \Delta x)}{\Delta x^{d-1}}\right) + \mathcal{O}\left(\frac{\Delta t}{\Delta x}\frac{\Delta t}{\Delta x^{d-1}}\right)\right] \\
&= \underbrace{\mathcal{O}(1) + \mathcal{O}(\Delta t) + \mathcal{O}(\Delta x)}_{K \in \Omega_{s,h}^{n+1} \cap \Omega_{s,h}^{n}} + \underbrace{\mathcal{O}(\Delta t) + \mathcal{O}(\Delta x)}_{K \in DC} + \underbrace{\mathcal{O}(\Delta t)}_{K \in FC} \\
&= \mathcal{O}(1) + \mathcal{O}(\Delta t) + \mathcal{O}(\Delta x).
\end{aligned} \tag{38}$$

Comparing this relation to Eq. (25), one can notice that the term associated to the DCs no longer depends on $\frac{1}{\Delta t}$ and that the dependency on Δx is linear instead of quadratic.

4.3. Numerical validation on SFO

As in the previous Section 3.3, the impact of the RG formulation is investigated on the convergence in space and time of the SFO with the Seo and Mittal's test case [34]. Here we consider the base and linear models.

4.3.1. Regularized base model

The results of the RG base model in comparison of the standard base model for the DF are displayed on Fig. 11. It is quite obvious to notice the dramatic decrease of the SFO by using the RG formulation instead of the original approach.

As previously, $C_P^{2\delta}$ is used to quantify the SPO amplitude, cf. Eq. (26). Fig. 12 shows $|C_P^{2\delta}|$ plotted as a function of grid spacing and time-step for both the RG and standard DF base models. It is noted that there is at least a difference of one order of magnitude between both the formulations at a given time-step and grid spacing. Then, $C_{P,\sigma}^{2\delta}$ and $C_{P,Max}^{2\delta}$ are plotted as a function of grid spacing in Fig. 13 and time-step in Fig. 14. We denote these quantities by $Cp_{\star,\sigma}^{2\delta}$ and $Cp_{\star,Max}^{2\delta}$ where $\star$ stands for the standard or regularized version. When considering time and space variations around $\Delta t = \Delta t_0$, cf. Fig. 13(a), and $D/\Delta x = 16$, cf. Fig. 14(a), they can be fitted by the following power-law:

$$Cp_{RG,\sigma}^{2\delta} = \Delta t^{0.377}\Delta x^{0.9493} \quad \text{and} \quad Cp_{RG,Max}^{2\delta} = \Delta t^{-0.0055}\Delta x^{1.1782}. \tag{39}$$

In Section 3.3, we concluded that, in the configurations where the SFO can have a large amplitude (coarse grid spacing, little time-steps), the main term is of order $\mathcal{O}\left(\frac{\Delta x^2}{\Delta t}\right)$ and well represented by $Cp_{DF,Max}^{2\delta}$. Here, we expect that this dependence will be changed in $\mathcal{O}\left(\frac{\Delta t}{\Delta x}\frac{\Delta x^2}{\Delta t}\right) = \mathcal{O}(\Delta x)$ due to the introduction of $\tau \propto \frac{\Delta t}{\Delta x}$.

This dependence is confirmed concerning the space convergence on Fig. 13(a)–(c) for various fixed time-steps, and concerning the time-step convergence on Fig. 14(a) and (b) for various fixed grid spacing. Indeed, the pressure peaks, measured by $C_{P,Max}^{2\delta}$, have no more dependence in the time-step when the grid spacing is coarse, explaining the null time-step and the one spatial order convergences for $Cp_{RG,Max}^{2\delta}$.

Concerning $Cp_{RG,\sigma}^{2\delta}$, the spatial convergence order is conform to the analysis, but the time-step order do not follow particularly Eq. (38). However, Eq. (38) shows a contribution proportional to $\mathcal{O}(\Delta t)$ leading to a time-step dependence of $Cp_{RG,\sigma}^{2\delta}$ as it measures all the contributions (FC and DC) to the SPO. This is the case in Fig. 14(a)–(b), even if the order is lower than one precisely because all the contributions are not proportional to $\mathcal{O}(\Delta t)$.

4.4. Regularized linear model

This subsection is devoted to the study of the impact of the linear-interpolation scheme on the pressure spurious oscillations. Even tough this procedure enables to gain one order of numerical rate of convergence in space leading in theory to more precise physical results for a same mesh refinement, it is necessary to assess its impact on the SFO by using once again the Seo and Mittal test case.

The results are presented on Fig. 15 for the standard and the RG versions of the DF. It can be noted that the linear interpolation procedure leads to $Cp_{DF,linear,Max}^{2\delta}$ values smaller than the $Cp_{DF,base,Max}^{2\delta}$ ones. As for the base model, the RG process decreases the $C_{P,Max}^{2\delta}$ values for the linear interpolation also. But this regularization is far away more efficient for the base model than for the linear model. Hence, the $Cp_{RG,base,Max}^{2\delta}$ values are the smallest ones.

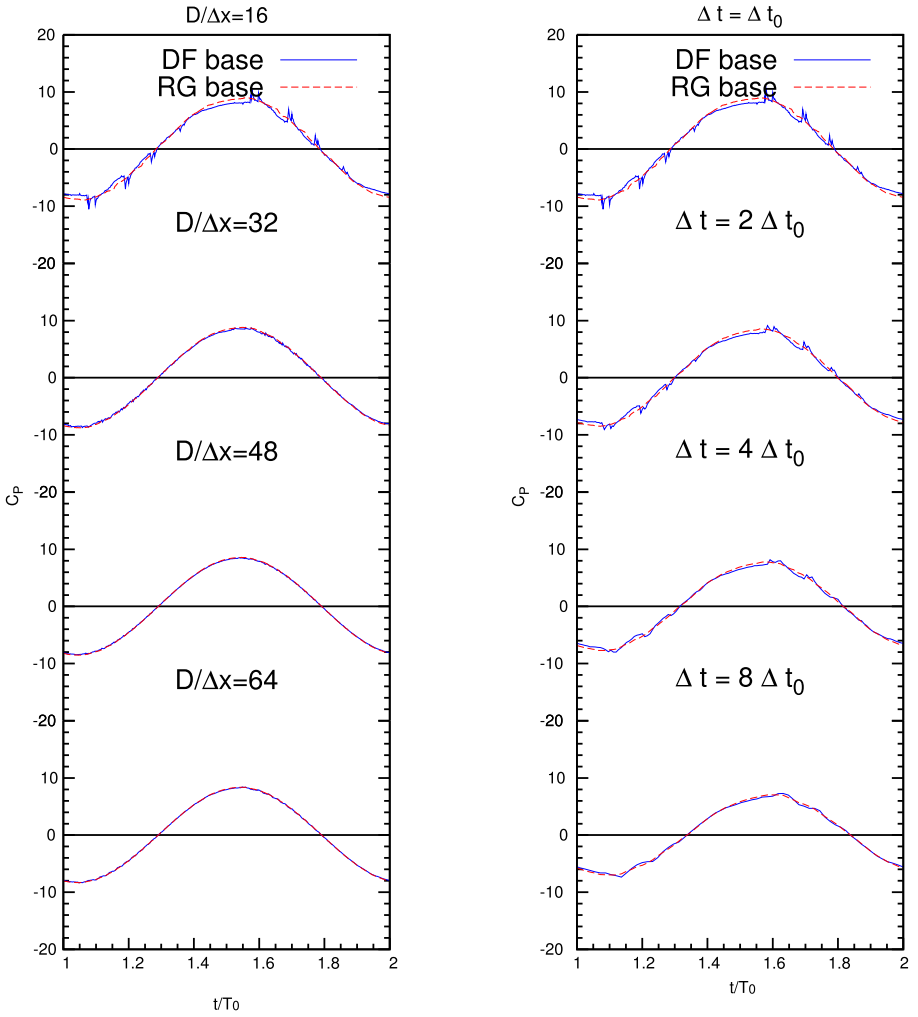

Fig. 11. C_P time histories for the Seo and Mittal's test case and the base model: (a) $\Delta t = \Delta t_0 = 0.002T_0$ for different grid spacing and (b) $D/\Delta x = 16$ for different time-steps. DF base: standard DF. RG base: regularized DF.

We can notice that, for the linear interpolation scheme, we obtain space convergence orders of $C^{2\delta}_{P,Max}$ higher than for the base scheme. This stands for the standard and the regularized DF. Without a theoretical analysis as done for the base scheme, we can only conjecture a link with the fact that the standard and RG DFs equipped with a linear formulation are second order accurate in space, cf. Section 5.1.

4.5. Conclusion

By comparing our results to the literature and particularly to Fig. 14 in [34], it is found that the $C^{2\delta}_{P,\sigma}$ is decreased by roughly one order of magnitude when using the standard DF base model (Figs. 13(a) and 14(a)) in comparison with their original method. Then, using the RG base model enables to gain at least one (or two; depending on the space and time resolutions) additional order of magnitude leading to similar level of SFO in comparison with their cut cell method. The main difference lies in the implementation as the RG base model is far more easy to implement than a cut-cell method.

Also, let us notice that the present results compare well with the ones of Lee et al. (Fig. 15 in [33]). They consider only the space-step evolution of the SFO's RMS. For common $\Delta X/\Delta X_0 \in [0.16; 0.64]$, our RG base-model results ($C^{2\delta}_{P,\sigma}$, Fig. 13) as well as our RG linear-model results ($C^{2\delta}_{P,\sigma} \leq C^{2\delta}_{P,Max}$, Fig. 15) are in the same range of values as that of Lee et al. (or lower).

5. Numerical and physical validation

This section is devoted to the numerical and physical validation of the RG base and linear models and the comparison with the results of the standard DF ones. Three cases have been selected by increasing gradually the complexity of the physical

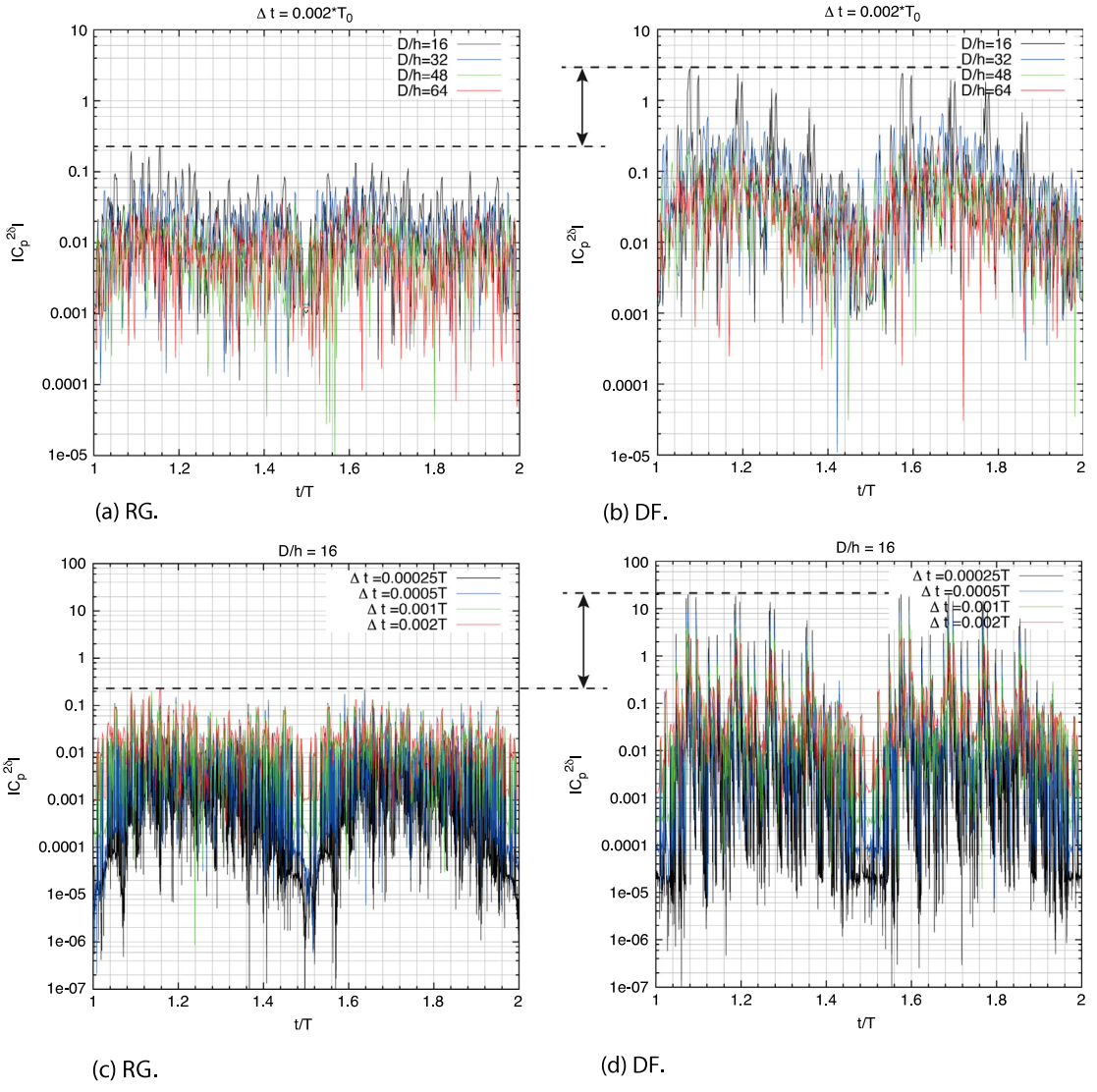

Fig. 12. $|C_P^{2\delta}|$ time histories for the Seo and Mittal's test case and the base model: (a, b) $\Delta t = \Delta t_0 = 0.002T_0$ for different grid spacing and (c, d) $D/\Delta x = 16$ for different time-steps. RG (resp. DF) denotes the regularized DF method (resp. the standard DF method).

phenomena at stake from a laminar cylindrical Couette flow to a cylinder with an imposed sinusoidal motion subjected to a cross-flow.

5.1. Numerical validation

Our goal is to assess the numerical rate of convergence of the standard and the proposed RG DF methods without (base model) and with the interpolation scheme, by doing a grid convergence study. A cylindrical Couette flow is considered and the results compared to the analytic solution by calculating the relative $L^2(\Omega_f)$ norm ϵ_2 of the error given by:

$$\epsilon_2 = \sqrt{\frac{\sum_{i=0}^{N_f}(u^i - u^i_{ref})^2}{\sum_{i=0}^{N_f} {u^i_{ref}}^2}} \tag{40}$$

where the superscript i denotes the ith face of the Eulerian grid, u^i_{ref} a reference velocity calculated on the ith face thanks to the analytic solution and N_f the total number of faces in the fluid region Ω_f.

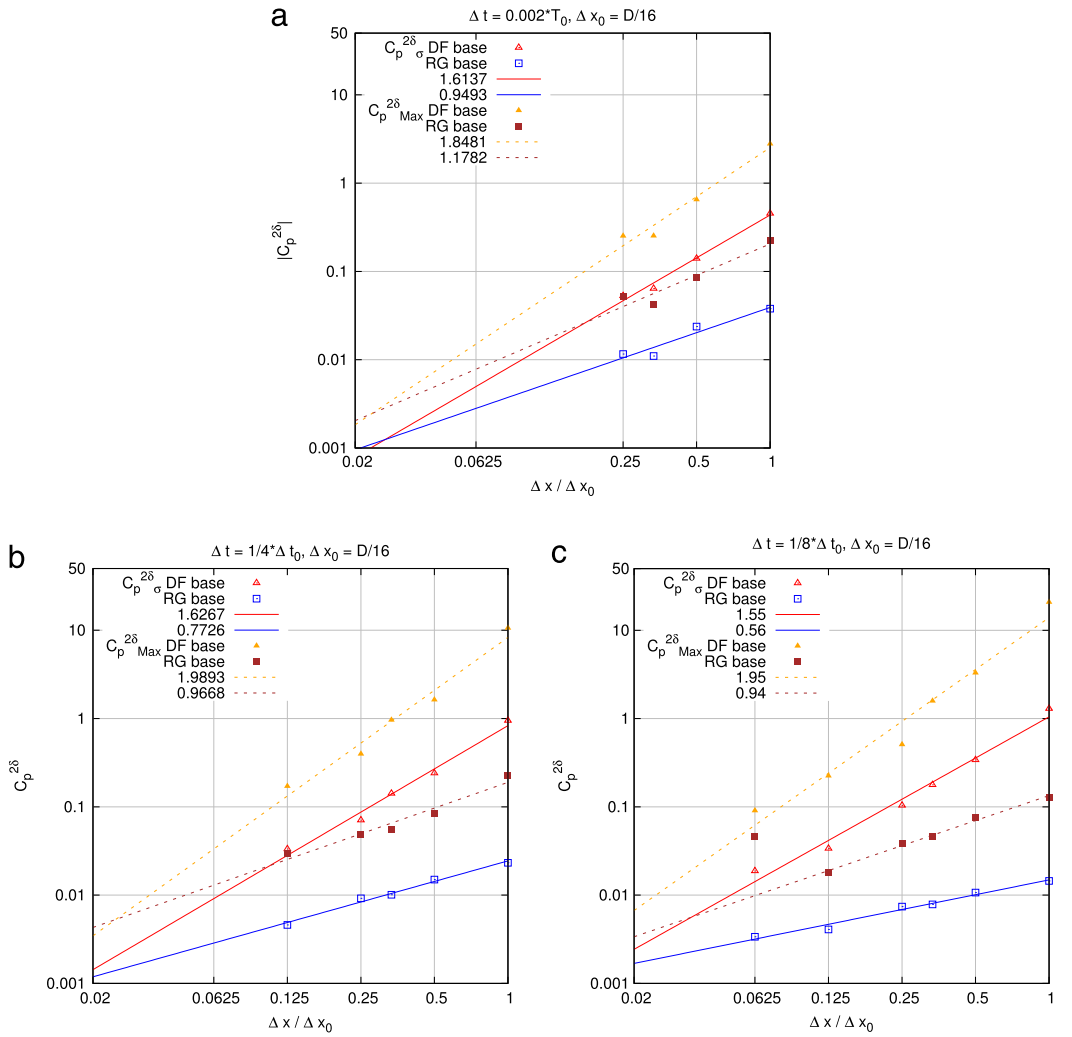

Fig. 13. $C_{P,\sigma}^{2\delta}$ and $C_{P,Max}^{2\delta}$ for the Seo and Mittal's test case versus grid spacing: (a) $\Delta t = \Delta t_0 = 0.002T_0$, (b) $\Delta t = \frac{1}{4}\Delta t_0$ and (c) $\Delta t = \frac{1}{8}\Delta t_0$.

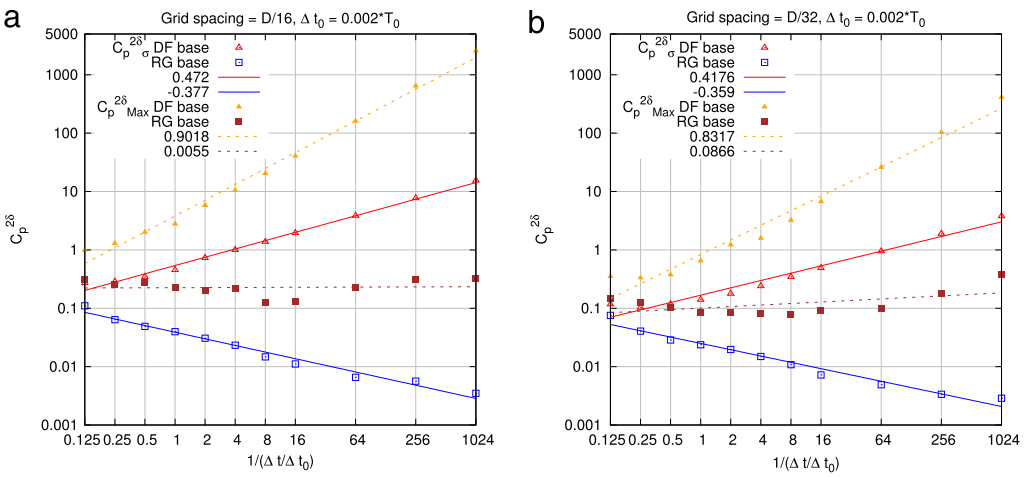

Fig. 14. $C_{P,\sigma}^{2\delta}$ and $C_{P,Max}^{2\delta}$ for the Seo and Mittal's test case versus time-steps: (a) $D/\Delta x = 16$ and (b) $D/\Delta x = 32$.

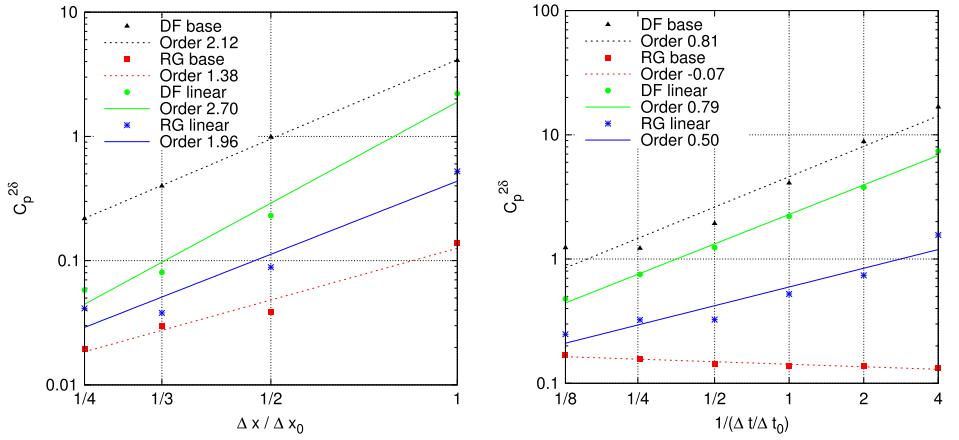

(a) Space convergence of $C^{2\delta}_{P,Max}$ for $\Delta t_0 = 0.002T_0$. (b) Time convergence of $C^{2\delta}_{P,Max}$ for $\Delta x_0 = D/16$.

Fig. 15. $Cp^{2\delta}_{Max}$ for the base and the linear interpolation schemes for both the DF and RG formulations.

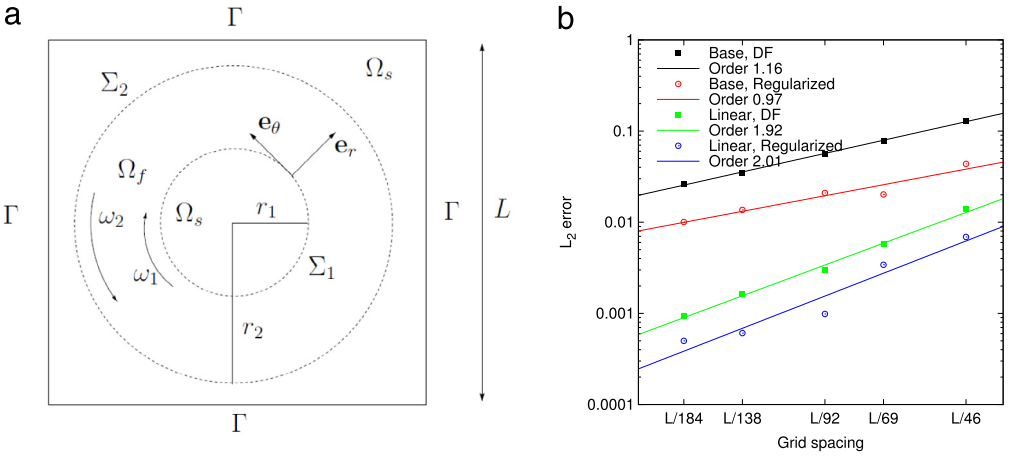

Fig. 16. Cylindrical Taylor–Couette problem: (a) computational domain and (b) relative $L^2(\Omega_f)$ norm of the error vs. the ratio of the domain length L over the number of elements. The CFL number is set to 1. Comparison of the base model with the interpolation model for both the standard and the regularized direct forcing.

This problem has already been considered in the frame of IBMs [40,43,44]. It allows to numerically estimate the order of spatial accuracy of the proposed methods on problem involving rotating geometries.

Fig. 16(a) presents the geometrical features of the computational domain $\Omega = [0, L] \times [0, L]$ composed of the solid and fluid domains: $\Omega = \Omega_s \cup \Omega_f$. The immersed boundaries Σ_1 and Σ_2 mimic the inner and outer cylinders of radius r_1 and r_2. The inner cylinder rotates clockwise ($\omega_1 > 0$) while the outer cylinder rotates in the counterclockwise ($\omega_2 < 0$). In all calculations, we assume the Reynolds number $Re = \frac{|\omega_1| r_1^2}{\nu}$ to be set to 1. Then, the Taylor number $Ta = 0.5Re^2 \frac{(r_1+r_2)(r_2-r_1)^3}{r_1^4}$ is $\frac{3}{2} < Ta_c$ where $Ta_c \approx 1.712$ is the critical Taylor number [45]. This assumption implies a strictly 2D flow.

Fig. 16(b) presents the $L^2(\Omega_f)$ norm ϵ_2 defined by Eq. (40). A quasi-linear numerical rate of convergence is obtained for the base model and a quasi-quadratic rate for the linear interpolation scheme for both the DF and the RG formulations. These results confirm the enhancement of accuracy expected with the linear interpolation model, and show that the regularization method do not deteriorate the convergence order.

5.2. Physical validation

A static cylinder in a cross-flow with $Re = 100$ and an imposed sinusoidal-motion cylinder subjected to a cross-flow of Reynolds number $Re = 185$ have been selected for the physical validation. Here we focus on physical parameters such as hydrodynamic coefficients.

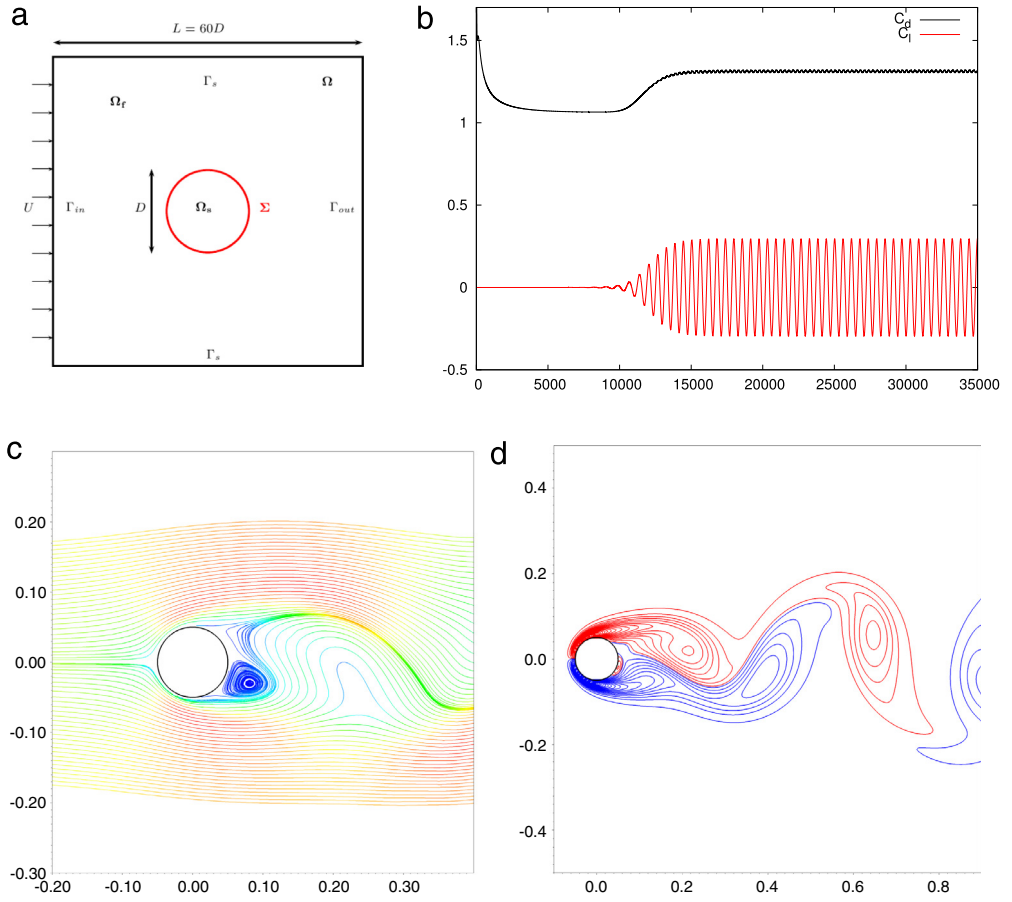

Fig. 17. Static cylinder in a cross-flow with $Re = 100$: (a) schematic representation of a fictitious computational domain Ω on a Cartesian grid with the solid domain Ω_S, the liquid domain Ω_f and the immersed boundary Σ, (b) time history of the hydrodynamic coefficients C_D and C_L, (c) streamlines and (d) vorticity. Standard base-model DF method with a computational domain and grid spacing ratio of $L/D = 60$ and $D/\Delta x = 25$.

5.2.1. Static cylinder in a cross-flow

We consider in this subsection the classic test case of a static circular cylinder in a cross-flow. The flow is characterized by the Reynolds number $Re = \frac{UD}{\nu}$ where U is the incoming velocity, D the cylinder diameter and ν the kinematic viscosity of the fluid. The simulations are performed in the unsteady laminar regime with $Re = 100$. The computational domain Ω, illustrated in Fig. 17(a), corresponds to a square of length L with a centered immersed cylinder. The boundaries of the computational domain $\partial\Omega$ must be located sufficiently far enough to reduce the impact of boundary conditions on vortex development behind the cylinder. Thus, the ratio L/D is set to 60. Symmetry conditions are prescribed on Γ_S, imposed velocity at the inlet and imposed pressure at the outlet. The hydrodynamic coefficients considered in this study are the drag $C_D = \frac{F_x}{0.5\rho U^2 D}$ and the lift $C_L = \frac{F_y}{0.5\rho U^2 D}$ with $(F_x, F_y)^t$ the fluid mechanical constraint integrated on Σ. The results are compared quantitatively in terms of these hydrodynamic coefficients and confront with Introïni et al. [40] that developed a penalized direct forcing method, quite similar to ours, of order 2 in space. Three uniform Cartesian grids are set, ranging from $D/\Delta x = 12.5$ to $D/\Delta x = 50$ with Δx the size of the Cartesian cells.

Fig. 17(b) gives an illustration of the type of C_D and C_L signals obtained by the simulations with $D/\Delta x = 12.5$ and the standard base-model DF method. The streamlines and the vorticity are displayed on Fig. 17(c) and (d). The periodic regime is reached after roughly 25 periods. Consequently, the computation of the time average $\overline{C_\star}$ and the amplitude $C_\star'$ of the signal $C_\star$ is systematically done after 30 periods. They are calculated thanks to the standard deviation $\sigma_{C_\star}$ by the following relation: $C_\star' = \sqrt{2}\sigma_{C_\star}$ as C_D and C_L are harmonic signals. Table 1 presents the results of the linear interpolation schemes for $D/\Delta x = 25$ and Fig. 18 in their entirety.

Qualitatively, both the standard and the RG formulations of the (base or linear) DF method have the same trend when refining the mesh. That is coherent with the way the RG formulation is implemented. Quantitatively, whatever formulation is considered (standard or RG linear), the time-averaged drag and the drag and lift amplitudes are well calculated with less than 2%–5% of relative deviation for the finest mesh.

Given the results obtained for this test case, it can be emphasized that the RG formulation does not alter the hydrodynamic coefficients values. In fact, the RG linear DF provides even better results than the standard linear DF.

Table 1
Hydrodynamic coefficients associated with the problem of unsteady flow around a static cylinder, $Re = 100$ and $D/\Delta x = 25$.

	$D/\Delta x = 25$ and $L/D = 60$				$D/\Delta x = 50$and $L/D = 60$	
	Stand. linear	Relat. deviation vs. [40] (%)	RG linear	Relat. deviation vs. [40] (%)	Introïni et al. [40]	Range [40]
$\overline{C_D}$	1.3890	3.1	1.3777	2.3	1.347	1.317–1.392
C'_D	0.01013	12.6	0.009512	5.7	0.009	0.009–0.012
C'_L	0.3429	5.2	0.3338	2.4	0.326	0.303–0.349
St	0.165	<0.2	0.165	<0.3	0.165	0.164–0.172

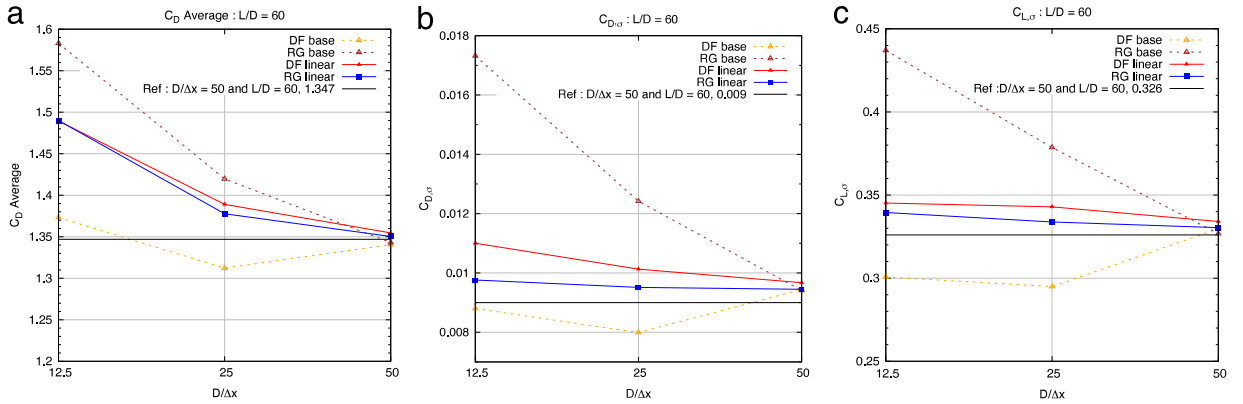

Fig. 18. Static cylinder in a cross-flow with $Re = 100$: (a) time-averaged drag, (b) drag amplitude and (c) lift amplitude for both the standard and the RG formulations. Comparison with the results of Introïni et al. [40] ($L/D = 60$ and $D/\Delta x = 50$).

5.2.2. Oscillating cylinder in cross-flow

The effect of the cylinder motion on the hydrodynamic coefficient values is investigated on this test case. We expect that the RG formulation should improve the results in comparison with the original one as it cut off the force oscillations. This test case consists in one of the numerical experiments conducted by Guilmineau and Queutey [46]: a circular cylinder with an imposed harmonic motion. As for the static cylinder, the flow is characterized by the Reynolds number $Re = \frac{UD}{\nu}$. The simulations are performed in the unsteady laminar regime with $Re = 185$. The boundary conditions and the computational domain are the same as for the static cylinder test case.

The imposed sinusoidal motion is defined by:

$$\begin{cases} x_c(t) = x_c(0) + A_e \cos(2\pi f_e t) \\ y_c(t) = y_c(0) \end{cases}$$

where $(x_c(0), y_c(0))^t$ are the initial coordinates of the cylinder, A_e the amplitude of the oscillation and f_e its frequency.

Simulations are performed for ratios of $A_e/D = 0.2$ and $f_e/f_0 = 1.1$ where f_0 is the natural shedding frequency from the stationary cylinder at $Re = 185$. From [46], we set $St_0 = \frac{f_0 D}{U} \approx 0.19$ with U the incoming velocity. Then our reference Strouhal number is $St_{ref} = 1.1\,St_0 \approx 0.209$. Here again, three uniform Cartesian grids are set characterized by: $D/\Delta x = 12.5$, $D/\Delta x = 25$ and $D/\Delta x = 50$. Fig. 19(a) and (b) give an illustration of the flow physic, displaying the stream lines and the vorticity around the circular cylinder when it reaches its upper position. The results are compared quantitatively in terms of hydrodynamic coefficients and confront with the results from Guilmineau and Queutey [46]. In this test case, the time-averaged drag coefficient $\overline{C_D}$ and the standard deviations $C_{D,\sigma}$ and $C_{L,\sigma}$ of the drag and lift are considered.

Fig. 20 does a comparison between the standard and the RG methods equipped with the base model in term of force oscillations for the coarsest space-step $D/\Delta x = 12.5$. It can be clearly noticed that the RG formulation decreases drastically the force oscillations without altering the physics. This is qualitatively confirmed by a comparison between the drag and lift coefficients over a few periods of time obtained by the RG-linear DF method and by Guilmineau and Queutey, cf Fig. 21.

Table 2 shows the values of the hydrodynamic coefficients computed with the linear model and a grid spacing ratio of $D/\Delta x = 25$. The results for all the mesh sizes and both the formulations are displayed on Fig. 22. As a whole, for a given hydrodynamic coefficient, all the computations converge in space toward the same value as expected. The standard and RG DF formulations retain the same behavior when decreasing the grid size. We conclude that the RG formulation is able to reduce the SFO while providing good results in comparison with the literature. The relative deviation of the hydrodynamic coefficients remains lower than 3% (resp. 9%) for $\overline{C_D}$ and $C_{L,\sigma}$ (resp. $C_{D,\sigma}$).

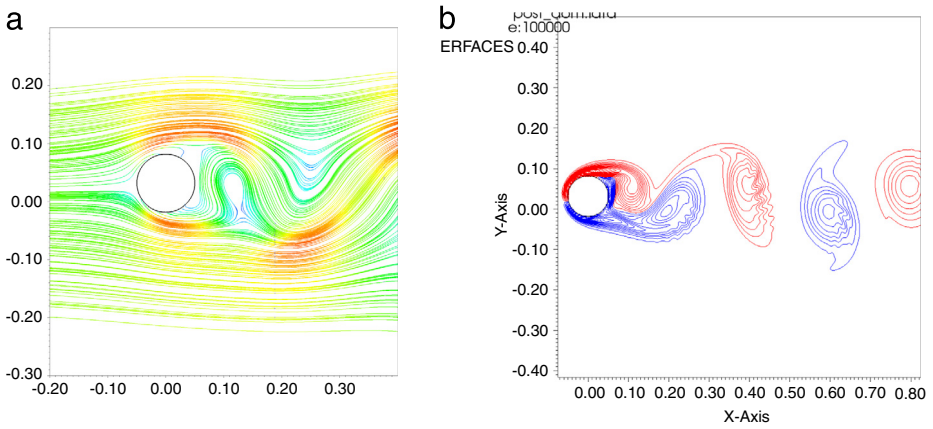

Fig. 19. Unsteady flow around a cylinder in a harmonic motion: (a) stream lines and (b) vorticity for the RG linear formulation when the cylinder is at its upper position. The stream lines are colored in function of the velocity along the x axis value. The vorticity red lines are negative and the blue ones are positive. (For interpretation of the references to color in this figure legend, the reader is referred to the web version of this article.)

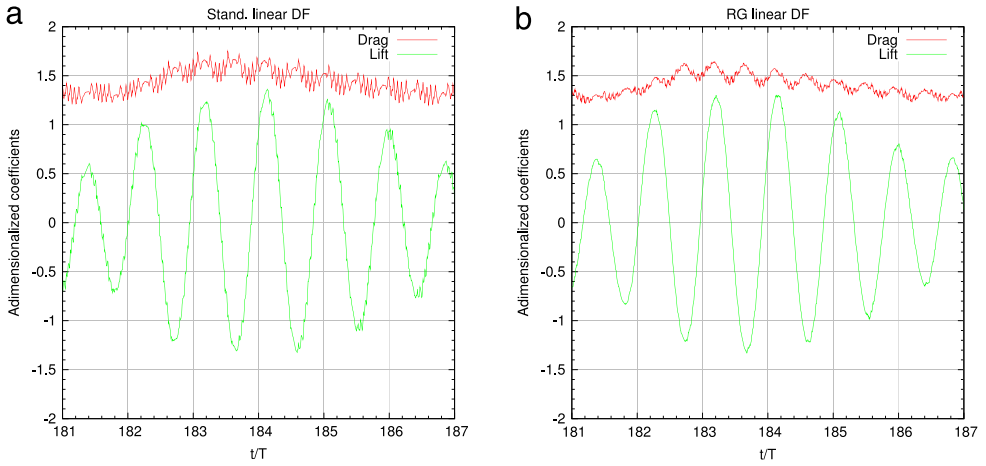

Fig. 20. Time history of the drag and lift coefficients over a period of time for (a) the standard linear and (b) the RG linear formulations with a computational domain of $L/D = 60$ and a grid spacing ratio of $D/\Delta x = 12.5$; $T = 1/f_e$.

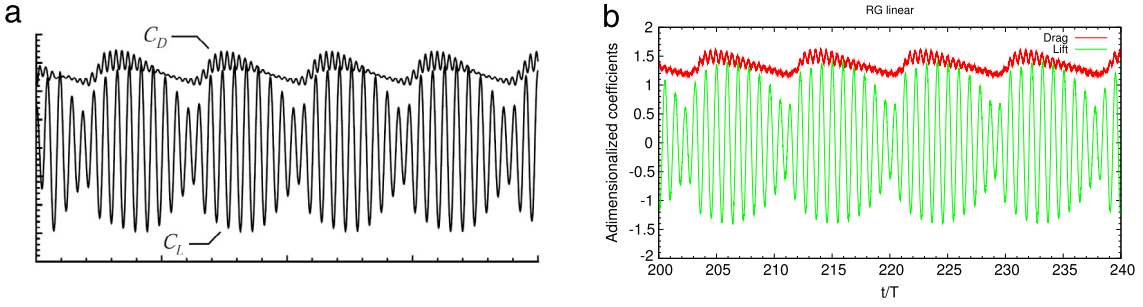

Fig. 21. Comparison of the drag and lift coefficients over a few periods of time: (a) picture from the article of Guilmineau and Queutey [46] and (b) results from the RG-linear formulation with a computational domain of $L/D = 60$ and a grid spacing ratio of $D/\Delta x = 25$; $T = 1/f_e$.

6. Summary

The main goal of this article was twofold. First, we have driven a theoretical analysis of the dependency to space and time steps of the SFO magnitude observed in the simulations of moving boundary problems with sharp-interface IBM. The SFO decreases by decreasing the grid spacing and increasing the time-step. Second, we have presented a regularized formulation of the DF method, capable of cutting off the SFO. As the standard DF, it consists in solving the Navier–Stokes equations on a Cartesian grid by adding a direct forcing term that mimics the presence of the solid. But here, the forcing term is

Table 2
Hydrodynamic coefficients associated with the problem of unsteady flow around a cylinder in a harmonic motion [46], $Re = 185$ and $D/\Delta x = 25$. Our reference Strouhal number is $St_{ref} = 1.1\,St_0 \approx 0.209$.

	$L/D = 60$				$L/D = 50$
	Stand. linear	Relative deviation vs. [46] (%)	RG linear	Relative deviation vs. [46] (%)	Guilmineau et al. [46]
$\overline{C_D}$	1.415	0.4	1.366	3.8	1.42
$C_{D,\sigma}$	0.134	10	0.119	20	0.149
$C_{L,\sigma}$	0.844	5.9	0.840	6.4	0.897
St	0.203	2.9 vs. St_{ref}	0.206	1.4 vs. St_{ref}	0.214

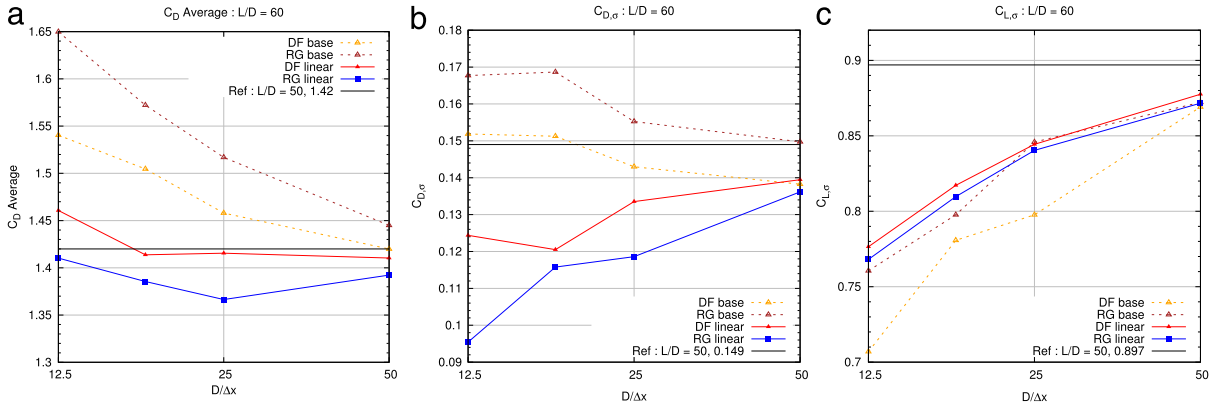

Fig. 22. Unsteady flow around a cylinder in a harmonic motion [46]: (a) time-averaged drag, (b) drag standard deviation and lift standard deviation for both the standard and the RG formulations of the DF method (base and linear models) in comparison with results from Guilmineau and Queutey [46].

regularized through an appropriated weighting. Contrary to the simple solid volume fraction weighting, the expression of the regularizing function of the forcing term is carefully chosen to smooth the fluid temporal discontinuity through the fluid–solid interface leading to a dramatic reduction of the SFO without altering the physical phenomena at stake. Concerning the design of the immersed boundary condition for the velocity, the RG formulation introduces an explicit-in-time weighting between the values resulting from the interpolation scheme and from the flow-solver numerical scheme. This velocity mixing is explicit: that is no iteration is run to get an implicit mixing between the two velocities as in [30,31], leaving the *native* numerical scheme of a given code unchanged. Here, two interpolation schemes have been considered: the direct solid velocity affectation and the linear interpolation from [40].

To assess the spatial and time dependencies of the oscillation amplitude, an analysis has been conducted to predict the variation of the forcing term for the standard and RG DF methods with a first-order interpolation model. Concerning the standard DF method, the SFO behavior is found in $\mathcal{O}(\frac{\Delta x^2}{\Delta t}) + \mathcal{O}(\Delta x)$ due to the DCs that bring the main contribution. For small time-steps, this is in good agreement with the literature: $\mathcal{O}(\frac{\Delta x^2}{\Delta t})$ [33] or $\mathcal{O}(\frac{\Delta x^d}{\Delta t})$ [34]. Concerning the RG DF method, the SFO behavior is found in $\mathcal{O}(\Delta t) + \mathcal{O}(\Delta x)$. As the term $\mathcal{O}(\frac{\Delta x^2}{\Delta t})$ is replaced by $\mathcal{O}(\Delta t)$, it comforts the fact that the RG formulation decreases the spurious force oscillations. Then, the analysis results have been confronted to the numerical test case of Seo and Mittal [34], an oscillating cylinder in a fluid at rest with a Reynolds number of about 78, using both the original and the RG approaches, by quantifying the SFO thanks to the pressure-drag 2-δ discontinuity. The numerical spatial and time dependencies of the oscillations are very close to the theoretical ones predicted by our analysis for the standard and the RG DF methods.

From a general point of view, the RG approach decreases the oscillations by at least one to two orders of magnitude over a large range of grid spacing and time-step without increasing the computational cost. The results obtained in this matter are quite similar to [34] that used a cut-cell method that is much more complicated to implement.

Through the numerical simulation of the academical test case of the laminar cylindrical Taylor–Couette flow [40], it results that the quadratic numerical rate of convergence in L^2 norm of the linear DF method is kept by the RG DF method.

At last, two numerical experiments have been conducted to assess the physical validity of the RG formulation: a static cylinder subjected to a cross-flow with a Reynolds number of 100 and a cylinder with an imposed sinusoidal motion subjected to a cross-flow of Reynolds number 185. When the solid is in motion, the RG formulation decreases dramatically the force oscillations especially when the time-step and/or the mesh refinement are quite low (*i.e.* $10 < D/\Delta x < 20$). Generally speaking, considering the hydrodynamic coefficients, the behavior of the original method tends to be the same as the RG formulation as expected when refining the mesh. It is coherent with their implementations.

These results are quite in good agreement with the literature and prove that the RG linear method is capable of computing complex fluid flows around moving boundaries.

Concerning our field of applications, this work constitutes a first step toward more complicated FSI problems in two-phase flows such as the fluid–elastic instability of moving tubes in a tube bundle subjected to a transverse two-phase flow. Indeed, the regularized direct forcing approach adopted in this article is easy to couple with ingredients for this kind of simulations as level-set methods using, for instance, the Després–Lagoutière scheme for advection [47] on the fluid density.

References

[1] C. Farhat, M. Lesoinne, N. Maman, Mixed explicit/implicit time integration of coupled aeroelastic problems: three-field formulation, geometric conservation and distributed solution, Internat. J. Numer. Methods Fluids 21 (1995) 807–835.
[2] C. Farhat, P. Geuzaine, C. Grandmont, The discrete geometric conservation law and the nonlinear stability of ALE schemes for the solution of flow problems on moving grids, J. Comput. Phys. 174 (2001) 669–694.
[3] V.K. Saul'ev, On the solution of some boundary value problems on high performance computers by fictitious domain method, Sib. Math. J. 4 (1963) 912–925.
[4] R.J. LeVeque, Z. Li, The immersed interface method for elliptic equations with discontinuous coefficients and singular sources, SIAM J. Numer. Anal. 31 (1994) 1019–1044.
[5] G. Yang, D.M. Causon, D.M. Ingram, R. Saunders, P. Batten, A Cartesian cut cell method for compressible flows Part A: Static body problems, Aeronaut. J. 101 (1997) 47–56.
[6] H. Johansen, Ph. Colella, A Cartesian grid embedded boundary method for Poisson's equation on irregular domains, J. Comput. Phys. 147 (1998) 60–85.
[7] Ph. Angot, A model of fracture for elliptic problems with flux and solution jumps, C. R. Acad. Sci., Paris, Ser. I 337 (2003) 425–430.
[8] I. Ramière, Ph. Angot, M. Belliard, A general fictitious domain method with immersed jumps and non-conforming structured mesh, J. Comput. Phys. 225 (2) (2007) 1347–1387.
[9] C. Peskin, Numerical analysis of blood flow in heart, J. Comput. Phys. 25 (1977) 220–252.
[10] Y.-H. Tseng, J.H. Ferziger, A ghost-cell immersed boundary method for flow in complex geometry, J. Comput. Phys. 192 (2003) 593–623.
[11] R. Mittal, H. Dong, M. Bozkurttas, F.M. Najjar, A. Vargas, A. von Loebbecke, A versatile sharp interface immersed boundary method for incompressible flows with complex boundaries, J. Comput. Phys. 227 (2008) 4825–4852.
[12] R. Glowinski, T.W. Pan, J. Peraux, A fictitious domain method for Dirichlet problem and applications, Comput. Methods Appl. Mech. Engrg. 111 (1994) 283–303.
[13] Ph. Angot, Ch.-H. Bruneau, P. Fabrie, A penalization method to take into account obstacles in incompressible viscous flows, Numer. Math. 81 (4) (1999) 497–520.
[14] I. Ramière, Ph. Angot, M. Belliard, A fictitious domain approach with spread interface for elliptic problems with general boundary conditions, Comput. Methods Appl. Mech. Engrg. 196 (4–6) (2007) 766–781.
[15] I. Ramière, Convergence analysis of the Q1-finite element method for elliptic problems with non-boundary-fitted meshes, Internat. J. Numer. Methods Engrg. 75 (9) (2008) 1007–1052.
[16] A. Sarthou, S. Vincent, J.-P. Caltagirone, Ph. Angot, Eulerian–Lagrangian grid coupling and penalty methods for the simulation of multiphase flows interacting with complex objects, Internat. J. Numer. Methods Fluids 56 (8) (2008) 1093–1099.
[17] B. Maury, A fat boundary method for the Poisson problem in a domain with holes, SIAM, J. Sci. Comput. 16 (3) (2001) 319–339.
[18] A. Duster, A. Niggl, E. Rank, Applying the hp-d version of the FEM to locally enhance dimensionally reduced models, Comput. Methods Appl. Mech. Engrg. 196 (2007) 3524–3533.
[19] D. Goldstein, R. Handler, L. Sirovich, Modeling a no-slip flow boundary with an external force field, J. Comput. Phys. 105 (2) (1993) 354–366.
[20] J. Mohd-Yussof, Combined Immersed Boundaries/B-Splines Methods for Simulations of Flows in Complex Geometries, CTR Annual Research Briefs, NASA Ames/Stanford University, 1997.
[21] E.A. Fadlun, R. Verzicco, P. Orlandi, J. Mohd-Yussof, Combined immersed-boundary finite-difference for three-dimensional complex flow simulations, J. Comput. Phys. 161 (2000) 35–60.
[22] T. Kajishima, S. Takiguchi, Interaction between particle clusters and particle-induced turbulence, Int. J. Heat Fluid Flow 23 (2002) 639–646.
[23] A. Gilmanov, F. Sotiropoulos, A hybrid Cartesian/immersed boundary method for simulating flows with 3D, geometrically complex, moving bodies, J. Comput. Phys. 207 (2005) 457–492.
[24] M. Uhlmann, An immersed boundary method with direct forcing for the simulation of particulate flows, J. Comput. Phys. 209 (2005) 448–476.
[25] D. Kim, H. Choi, Immersed boundary method for flow around an arbitrarily moving body, J. Comput. Phys. 212 (2) (2006) 662–680.
[26] J. Yang, E. Balaras, An embedded-boundary formulation for large-eddy simulation of turbulent flows interacting with moving boundaries, J. Comput. Phys. 215 (2006) 12–40.
[27] J.-I. Choi, R.C. Oberoi, J.R. Edwards, J.A. Rosati, An immersed boundary method for complex incompressible flows, J. Comput. Phys. 224 (2007) 757–784.
[28] X. Yang, X. Zhang, Z. Li, G. He, A smoothing technique for discrete delta functions with application to immersed boundary method in moving boundary simulations, J. Comput. Phys. 228 (2009) 7821–7836.
[29] C.-C. Liao, Y.-W. Chang, C.-A. Lin, J.M. McDonough, Simulating flows with moving rigid boundary using immersed-boundary method, Comput. & Fluids 39 (2010) 152–167.
[30] H. Luo, H. Dai, P. Ferreira de Sousa, A hybrid formulation to suppress the numerical oscillation caused by immersed moving boundaries, in: 62nd Annual Meeting of the APS Division of Fluid Dynamics, 2009, Abstract #EL.006.
[31] H. Luo, H. Dai, P. Ferreira de Sousa, B. Yin, On numerical oscillation of the direct-forcing immersed-boundary method for moving boundaries, Comput. & Fluids 56 (2012) 61–76.
[32] P.H. Chiu, R.K. Lin, T.W.H. Sheu, A differentially interpolated direct forcing immersed boundary method for predicting incompressible Navier–Stokes equations in time-varying complex geometries, J. Comput. Phys. 229 (2010) 4476–4500.
[33] J. Lee, J. Kim, H. Choi, K.S. Yang, Sources of spurious force oscillations from an immersed boundary method for moving-body problems, J. Comput. Phys. 230 (2011) 2677–2695.
[34] J.H. Seo, R. Mittal, A sharp-interface immersed boundary method with improved mass conservation and reduced spurious pressure oscillations, J. Comput. Phys. 230 (2011) 7347–7363.
[35] J. Lee, D. You, An implicit ghost-cell immersed boundary method for simulations of moving body problems with control of spurious force oscillations, J. Comput. Phys. 233 (2013) 295–314.
[36] C. Ji, A. Munjiza, J.J.R. Williams, A novel iterative direct-forcing immersed boundary method and its finite volume applications, J. Comput. Phys. 231 (2012) 1797–1821.
[37] J. Kim, D. Kim, H. Choi, An immersed-boundary finite volume method for simulations of flow in complex geometries, J. Comput. Phys. 171 (2001) 132–150.
[38] A.J. Chorin, Numerical solution of the Navier–Stokes equations, Math. Comp. 22 (1968) 745–762.
[39] R. Temam, Sur l'approximation de la solution des équations de Navier–Stokes par la méthode des pas fractionnaires, Arch. Ration. Mech. Anal. 32 (1969) 135–153.
[40] C. Introïni, M. Belliard, C. Fournier, A second order penalized direct forcing for hybrid Cartesian/immersed boundary flow simulations, Comput. & Fluids 90 (2014) 21–41.
[41] J.H. Ferziger, M. Peric, Computational Methods for Fluid Dynamics, Springer, New York, USA, 1996.
[42] J.L. Guermond, P.D. Minev, J. Shen, An overview of projection methods for incompressible flows, Comput. Methods Appl. Mech. Engrg. 195 (2006) 6011–6045.

[43] N. Peller, A. Le Duc, F. Tremblay, M. Manhart, High-order stable interpolations for immersed boundary methods, Internat. J. Numer. Methods Fluids 52 (2006) 1175–1193.
[44] Y. Cheny, O. Botella, The LS-STAG method: A new immersed boundary/level-set method for the computation of incompressible viscous flows in complex moving geometries with good conservation properties, J. Comput. Phys. 229 (2010) 1043–1076.
[45] E. Guyon, J.P. Hulin, L. Petit, Physical Hydrodynamics, Oxford University Press, Oxford, 2001.
[46] E. Guilmineau, P. Queutey, A numerical simulation of vortex shedding from an oscillating circular cylinder, J. Fluids Struct. 16 (2002) 773–794.
[47] B. Després, F. Lagoutière, Contact discontinuity capturing schemes for linear advection and compressible gas dynamics, J. Sci. Comput. 16 (4) (2001) 479–524.